

Orbital (Hydro)Climate Variability in the Ice-Free early Eocene Arctic

Chris Daniël Fokkema¹, Henk Brinkhuis², Francien Peterse¹, and Appy Sluijs¹

¹Utrecht University

²Royal NIOZ

April 08, 2024

Abstract

We explore the imprint of orbital variability on Arctic temperature and hydrology using sediments recovered during the Arctic Coring Expedition in 2004. High resolution records of lipid biomarkers (GDGTs; 2-kyr) and palynological assemblages (5-kyr) in the ~4 m interval below Eocene Thermal Maximum 2 (~54 Ma) show highly cyclic signals related to ~20-kyr precession, ~40-kyr obliquity and ~100-kyr eccentricity. The GDGTs indicate obliquity and precession variability representative of sea surface temperature (SST) variations up to ~1.4 and ~0.5 °C, respectively. Peak SSTs coincide with an elevated supply of pollen and spores and increased marine productivity. Together, this implies an orbital control on precipitation and terrestrial nutrient supply to the Arctic Basin. Assuming that SST maxima correspond to Arctic insolation maxima (precession minima/obliquity maxima), precipitation maxima also correspond to insolation maxima, implying regional hydrological processes as a forcing rather than variations in meridional water transport, starkly contrasting Pleistocene Arctic hydrology. The relative amplitudes of precession and obliquity in the SST record match that of local insolation between spring and fall, corroborating previous suggestions of a seasonal GDGT bias. The reconstructed complete orbital imprint refutes that ACEX temperature reconstructions are biased to one end of the orbital variability. Eccentricity-related SST variability was ~0.8 °C, ~2–3 times higher than synchronous variability in the deep ocean, and 3–4 times higher than similar variations in the tropics. This confirms eccentricity-forced global temperature variability during the Eocene, and that this had pronounced polar amplification, despite the absence of ice and snow albedo feedbacks.



1 **Orbital (Hydro)Climate Variability in the Ice-Free early Eocene Arctic**
2

3 **Chris D. Fokkema^{1*}, Henk Brinkhuis^{1,2}, Francien Peterse¹ and Appy Sluijs¹**

4 ¹ Department of Earth Sciences, Faculty of Geoscience, Utrecht University, 3584CB Utrecht,
5 The Netherlands

6 ² Royal Netherlands Institute for Sea Research (NIOZ), 1790 AB Den Burg, The Netherlands.

7 *Corresponding author: Chris D. Fokkema (c.d.fokkema@uu.nl)

8 **Key Points:**

- 9 • TEX₈₆-based early Eocene Arctic surface water temperatures (SSTs) depict obliquity and
10 precession imprints suggestive of a spring-to-fall forcing.
- 11 • Eccentricity forcing caused ~0.8 °C Arctic SST variability, showing strong Arctic amplification
12 despite absent albedo feedbacks.
- 13 • Precipitation maxima were in-phase with implied insolation maxima, suggesting a strong orbital
14 imprint on local hydrological processes.
15

16 **Abstract**

17 We explore the imprint of orbital variability on Arctic temperature and hydrology using
18 sediments recovered during the Arctic Coring Expedition in 2004. High resolution records of
19 lipid biomarkers (GDGTs; 2-kyr) and palynological assemblages (5-kyr) in the ~4 m interval
20 below Eocene Thermal Maximum 2 (~54 Ma) show highly cyclic signals related to ~20-kyr
21 precession, ~40-kyr obliquity and ~100-kyr eccentricity. The GDGTs indicate obliquity and
22 precession variability representative of sea surface temperature (SST) variations up to ~1.4 and
23 ~0.5 °C, respectively. Peak SSTs coincide with an elevated supply of pollen and spores and
24 increased marine productivity. Together, this implies an orbital control on precipitation and
25 terrestrial nutrient supply to the Arctic Basin. Assuming that SST maxima correspond to Arctic
26 insolation maxima (precession minima/obliquity maxima), precipitation maxima also correspond
27 to insolation maxima, implying regional hydrological processes as a forcing rather than
28 variations in meridional water transport, starkly contrasting Pleistocene Arctic hydrology. The
29 relative amplitudes of precession and obliquity in the SST record match that of local insolation
30 between spring and fall, corroborating previous suggestions of a seasonal GDGT bias. The
31 reconstructed complete orbital imprint refutes that ACEX temperature reconstructions are biased
32 to one end of the orbital variability. Eccentricity-related SST variability was ~0.8 °C, ~2–3 times
33 higher than synchronous variability in the deep ocean, and 3–4 times higher than similar
34 variations in the tropics. This confirms eccentricity-forced global temperature variability during
35 the Eocene, and that this had pronounced polar amplification, despite the absence of ice and
36 snow albedo feedbacks.

37

38 **Plain Language Summary**

39 During the early Eocene (56–48 million years ago), an ancient period of global high atmospheric
40 CO₂ concentrations and temperatures, the Arctic Ocean was an ice-free, (sub)tropical, semi-
41 enclosed basin. Our understanding of this unfamiliar Arctic situation relies largely on
42 geochemical and (micro)fossil analysis of sediments retrieved by the single academic drilling
43 expedition that recovered sediments from this period. However, the available temperature data of
44 the Eocene Arctic are insufficient to capture the climate variations caused by Earth's orbit (often
45 termed "Milankovitch cycles"), which are also responsible for the repeating occurrence of ice
46 ages over the past million years. Here, we reconstruct past Arctic temperatures using
47 temperature-sensitive molecular fossils in a 4-m thick sediment interval deposited during the
48 early Eocene on a 1-cm (~2,000-year) resolution. Our results show that Arctic surface
49 temperatures varied more than those at lower latitudes during global variations, and display 2 °C
50 variability corresponding to the local insolation changes resulting from precession and the tilt of
51 Earth's axis, with respective periods of 21,000 and 41,000 years. Changes in microfossil content
52 show that the warmer periods coincided with increased rainfall, indicating that moisture
53 availability at the poles was similarly forced on these timescales.

54

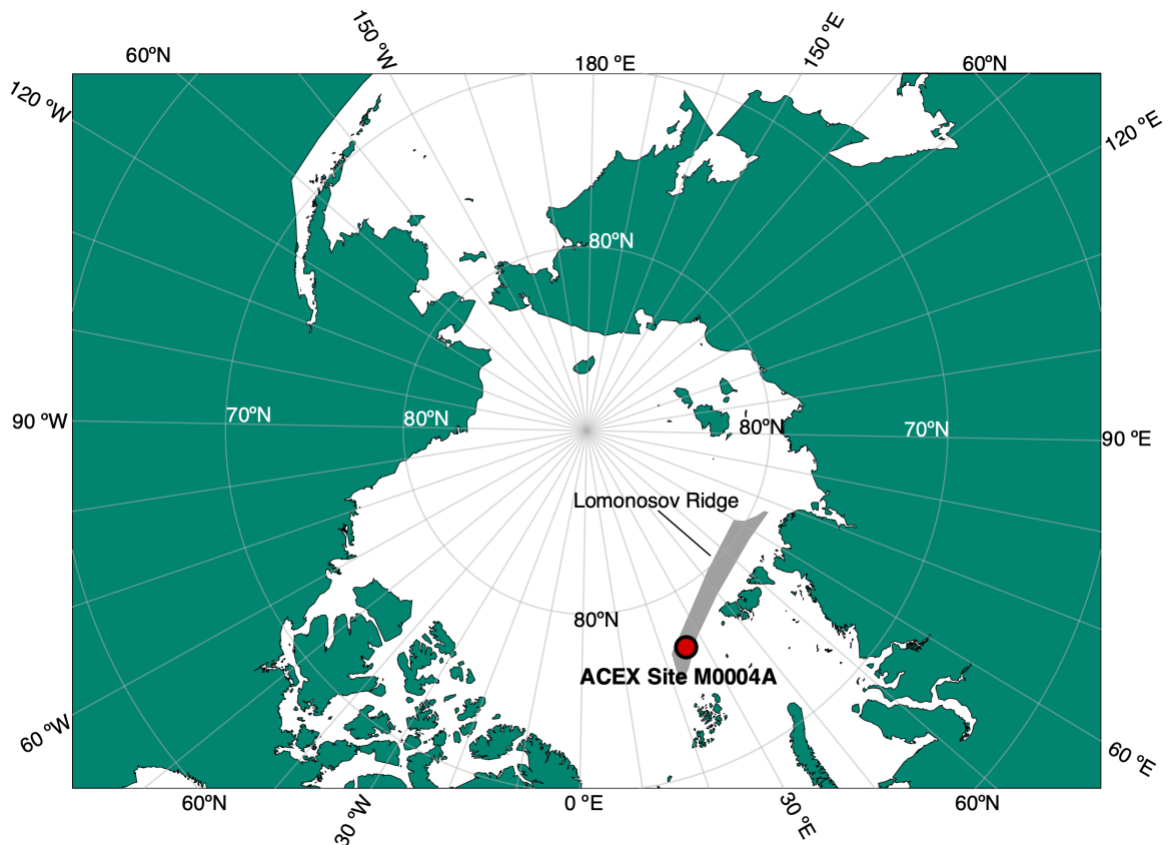
55 **1 Introduction**

56 Millennial-scale fluctuations of insolation induced by Earth's orbital parameters (i.e.,
57 Milankovitch cycles) are at their extremes at the poles, where obliquity forces changes up to
58 ~10% (~34 W/m²) of the annual average insolation, and precession up to ~20% (~80 W/m²) in

59 peak summer insolation (Laskar et al., 2004; Li et al., 2019). These Milankovitch variations —
60 also including orbital eccentricity that modulates the amplitude of precession — at the high
61 latitudes were responsible for the pacing of glacial-interglacial variability since the establishment
62 of a more permanent cryosphere at the Oligocene-Eocene transition (e.g., Westerhold et al.,
63 2020). In the Pleistocene, their regional impact on the sea surface temperature (SST) of the
64 Arctic Ocean was strongly reduced due to the high albedo and insulation of the sea ice cover, and
65 clipped at minimum SSTs of approximately $-2\text{ }^{\circ}\text{C}$ (e.g., Carton et al., 2015). Hypothetically, the
66 imprint of orbital forcing on Arctic SST is expected to be much larger in the absence of (sea)ice
67 during past "hothouse" climates. Furthermore, because the poles experience the maximum
68 seasonality of insolation — daily insolation at the poles ranges from zero in winter to values
69 exceeding tropical insolation in summer — an ice-free pole would imply a non-analog climate
70 state that experiences extreme seasonal SST variability.

71 The presence of significant ice sheets can be ruled out for the early Eocene (~56–48 Ma),
72 characterized by high atmospheric $p\text{CO}_2$ (Anagnostou et al., 2020) and high global mean
73 temperatures (Inglis et al., 2020). Overall warm climate in the early Eocene was accentuated by
74 multiple transient global warming events ("hyperthermals"), of which the Paleocene-Eocene
75 Thermal Maximum (PETM; 56 Ma (Kennett and Stott, 1991; Zachos et al., 2003; Sluijs et al.,
76 2006)) and Eocene Thermal Maximum 2 (ETM2; 54 Ma (Lourens et al., 2005; Sluijs et al.,
77 2009)) are best known. These events are globally marked by negative stable carbon isotope
78 ($\delta^{13}\text{C}$) excursions (CIEs) in organic and inorganic sedimentary components and deep ocean
79 acidification due to the release of ^{13}C -depleted carbon into the ocean-atmosphere system
80 (Dickens et al., 1995, 1997). The pattern and occurrence of these CIEs, as well as long-term $\delta^{13}\text{C}$
81 trends, combined with biostratigraphy, have proven to be excellent stratigraphic correlation tools,
82 which can be used to compare climatic variations associated with hyperthermals on global scales
83 (e.g., Cramer et al., 2003; Westerhold et al., 2018; Fokkema et al., 2023), and have been used to
84 prove that most, if not all, occur during maxima in the eccentricity of Earth's orbit (Lourens et
85 al., 2005; Galeotti et al., 2010; Lauretano et al., 2018).

86 Of key importance to understanding Paleogene climate and its hyperthermals has been
87 the Integrated Ocean Drilling Program (IODP) Expedition 302 in 2004, also known as the Arctic
88 Coring Expedition (ACEX). At IODP Site M0004 (paleolatitude 78°N , Fig. 1), ACEX recovered
89 an uppermost Paleocene to lower Eocene sequence comprised of organic-rich siliciclastic
90 mudstone from the Lomonosov Ridge (Backman et al., 2006). While the Paleogene sediments
91 are barren of calcareous and siliceous microfossils, they proved to be rich in lipid biomarkers and
92 palynomorphs (Backman et al., 2006). By combined organic walled dinoflagellate cyst
93 (dinocyst) biostratigraphy and $\delta^{13}\text{C}$ -chemostratigraphy, two CIEs (~384 meters composite depth
94 (mcd), Core 30X and ~369 mcd, Core 27X, respectively) were identified as the PETM and
95 ETM2 hyperthermal events (Stein et al., 2006; Sluijs et al., 2006, 2009).



96

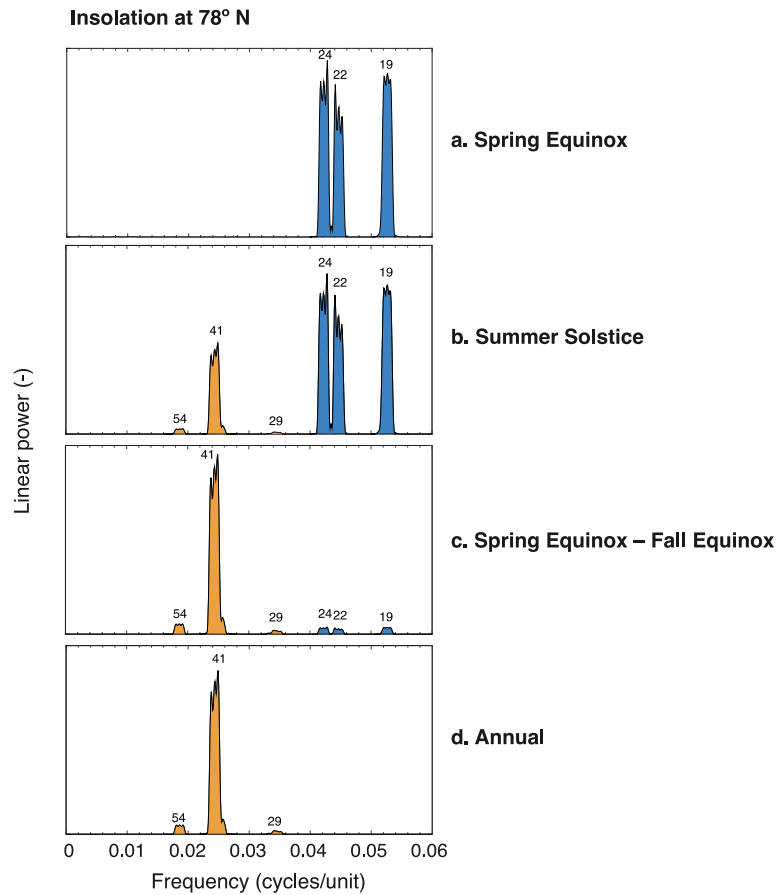
97 **Figure 1.** Paleogeographic map showing the position of ACEX Site M0004A (red dot) in the
 98 early Eocene Arctic Ocean on Lomonosov Ridge (grey area). Figure adapted from (Sluijs et al.
 99 (2020).

100 The TetraEther indeX of 86 carbon atoms (TEX₈₆) is a water temperature proxy based on
 101 the number of cyclic moieties in Nitrososphaeral (previously named "Thaumarchaeota" or
 102 "Crenarchaeota") membrane lipids termed glycerol dialkyl glycerol tetraethers (GDGTs)
 103 (Schouten et al., 2002). Application of this molecular paleothermometer at Site M0004A has
 104 revealed anomalously high Arctic SSTs exceeding 20 °C and reaching temperatures as high as 26
 105 °C and 27 °C during peak PETM and ETM2 (Sluijs et al., 2006, 2008b, 2009, 2020).
 106 Furthermore, these warming phases appeared associated with drastic environmental change. For
 107 example, the warming during both PETM and ETM2 led to wetter conditions in the Arctic,
 108 evidenced by increased low-salinity tolerant dinocysts and reduced proportions of terrestrial
 109 palynomorphs (Sluijs et al., 2006, 2008a, 2009). Accordingly, changes in the hydrogen isotope
 110 composition of plant waxes indicated increased poleward moisture transport during the
 111 hyperthermals that could have facilitated this increased rainfall (Pagani et al., 2006; Krishnan et
 112 al., 2014). Coeval presence of isorenieratene, a biomarker exclusively produced by green sulfur
 113 bacteria, points to photic zone euxinia, a consequence of enhanced freshwater stratification,
 114 warming and elevated terrestrial nutrient input in the basin (Sluijs et al., 2006, 2009). On land,
 115 the environmental extremes favored occurrence of megathermal floral taxa, including palms and
 116 even tropical baobab trees (Sluijs et al., 2009; Willard et al., 2019). These hydrological changes

117 were not unique to the Lomonosov Ridge margin, but a widespread Arctic phenomena, given
118 evidence from the, albeit nearby, Arctic Siberian margin (Suan et al., 2017).

119 The non-analog temperatures of the early Eocene Arctic region as well as the southern
120 high latitudes are historically problematic for climate models to explain under realistic CO₂
121 concentrations and/or meridional gradients, not only at the time of the early publications (e.g.,
122 Sluijs et al., 2006; Bijl et al., 2009), but even with the current state-of-the-art fully coupled
123 climate models (e.g., Evans et al., 2018; Cramwinckel et al., 2018; Lunt et al., 2021). Also
124 hydrological patterns appear challenging to simulate in accordance with proxy data
125 (Cramwinckel et al., 2023). However, the expected high amplitude of orbital climate variability
126 in an ice-free Arctic may imply that the existing (low-resolution) proxy records either represent
127 aliased climate signals, or climate signals that are biased towards one extreme of the variability.
128 For instance, sedimentation might have been biased towards the orbital configurations that led to
129 highest siliciclastic sediment supply, for which reconstruction of the complete orbital cycle
130 would potentially provide a less biased reconstruction of the climate signals. Moreover, while
131 TEX₈₆ is generally considered a proxy for mean annual SSTs, it was suggested that the export of
132 lipid biomarkers through fecal pelleting may have been biased towards the summer season
133 (Sluijs et al., 2006, 2020). Many of these concerns can be tested with higher-resolution
134 reconstructions, especially if orbital variability can be resolved. The patterns of orbital forcing on
135 insolation are characteristic per season and duration of the forcing (Fig. 2). For example, absence
136 of precession forcing in a climate parameter would imply a true annually averaged signal, while
137 absence of obliquity occurs during the equinoxes. Hence, the reconstruction of orbital cyclicity
138 in SST variations at the Lomonosov Ridge could help to put constrains on both the problem of
139 orbital clipping and seasonality of the signal.

140



141

142 **Figure 2.** Power spectra of insolation at 78 ° N, showing obliquity (orange) and precession (blue)

143 frequencies. (a) Insolation spectra during the spring equinox (~21 March). (b) Insolation spectra

144 during the summer solstice (~21 June). (c) Averaged insolation spectra between the spring and

145 fall equinoxes (~21 March – 22 September). (d) Mean annual averaged insolation spectra. All

146 spectra are calculated using the Multitaper Method in Acycle (Li et al., 2019) over insolation

147 curves for the past two million years (Laskar et al., 2004). Numbers above spectral peaks

148 indicate the corresponding periods in kyr.

149

150 Previous work on the ACEX sediments has identified orbitally forced patterns in

151 Paleogene sediments at the Lomonosov Ridge, including in the physical and geochemical

152 sediment properties (Sangiorgi et al., 2008; Pälike et al., 2008; Sluijs et al., 2008b), as well as

153 palynomorph assemblages (Sangiorgi et al., 2008; Barke et al., 2011). This work has shown that

154 sedimentation on the Lomonosov Ridge margin was significantly affected by climatic precession

155 and obliquity, likely mainly due to regional (hydro)climatic variability. Decimeter scale

156 variations in color and iron content in a laminated section, just below the ETM2 interval, have

157 been interpreted as precession and obliquity cycles (Sluijs et al., 2008b). However, apart from

158 XRF-based lithological indicators, the current environmental proxy data are of insufficient

159 temporal resolution to capture this orbital variability to its fullest and resolve any environmental

160 variability on these timescales.

161 Therefore, we here present the first high-resolution analyses of IODP Site M0004A Core
162 27X across the largely laminated interval covering ETM2 and the cyclic sediments below it
163 (~372–367.8 mcd). By utilizing combined lipid biomarkers and palynological datasets, we (1)
164 aim to detect the imprint of Milankovitch cycles on Arctic climate, (2) provide a quantitative
165 estimate of SST variability associated with the recorded orbital cycles using TEX₈₆, and (3)
166 provide a qualitative assessment of the hydrological change coupled to the temperature change
167 by assessing the abundance of terrestrial biomarkers and palynomorphs and low-salinity tolerant
168 dinocysts.
169

170 **2 Materials and Methods**

171 2.1 Site and sampling

172 Previous work on the ACEX sediments has identified orbitally forced patterns in
173 Paleogene sediments at the Lomonosov Ridge, including in the physical and geochemical
174 sediment properties (Sangiorgi et al., 2008; Pälike et al., 2008; Sluijs et al., 2008b), as well as
175 palynomorph assemblages (Sangiorgi et al., 2008; Barke et al., 2011). This work has shown that
176 sedimentation on the Lomonosov Ridge margin was significantly affected by climatic precession
177 and obliquity, likely mainly due to regional (hydro)climatic variability. Decimeter scale
178 variations in color and iron content in a laminated section, just below the ETM2 interval, have
179 been interpreted as precession and obliquity cycles (Sluijs et al., 2008b). However, apart from
180 XRF-based lithological indicators, the current environmental proxy data are of insufficient
181 temporal resolution to capture this orbital variability to its fullest and resolve any environmental
182 variability on these timescales.

183 2.2 Magnetic susceptibility

184 As a first order estimate of the iron content, magnetic susceptibility was measured on
185 each sample. For this, samples were first weighed in and measured for bulk magnetic
186 susceptibility, using a MFKF1-FA, with a precision better than $3.87 \times 10^{-8} \chi$.

187 2.3 Color analysis

188 High-resolution line-scan photographs (10 pixels/mm) of the archive halves (Backman et
189 al., 2006) were used to generate sediment color logs. For this, first, the cracks were removed
190 using the "DeCrack" program (Zeeden et al., 2015). Next, all remaining post-depositional
191 features were removed from the core pictures (e.g., bioturbation, secondary mineral phases,
192 drilling mud) using photo editing software. Finally, mean greyscale values were calculated on a 1
193 cm resolution with the "Colourlog" R-script (Kocken, 2022).

194 2.4 Lipid biomarkers

195 2.4.1 Lipid biomarker analysis

196 For the lipid biomarker analysis, on average 2 grams (ranging from 0.4 to 6.4 grams) of
197 powdered and homogenized sediment was extracted with 25 ml dichloromethane (DCM):MeOH
198 (9:1 v/v), using a Milestone Ethos X Microwave Extraction System for 50 minutes at 70 °C. A
199 known amount of C₄₆ glycerol trialkyl glycerol tetraether (GTGT) standard was added to each
200 lipid extract. The extracts were then passed over a NaO₂ column to remove any remaining water,

201 and dried under a gentle N₂ stream. The lipid extract was separated in an apolar, ketone and polar
 202 fraction over an activated Al₂O₃ column, utilizing hexane:DCM (9:1), hexane:DCM (1:1) and
 203 1:1 DCM:MeOH (1:1) as respective solvents. For GDGT analysis, the polar fraction was first
 204 dried under N₂, and then redissolved in 99:1 hexane:isopropanol, filtered through a 0.45 µm
 205 polytetrafluoroethylene filter and injected into an Agilent 1290 infinity ultra high-performance
 206 liquid chromatograph (UHPLC) coupled to an Agilent 6135 single quadrupole mass
 207 spectrometer using the method and instrument settings of [Hopmans et al. \(2016\)](#). Isoprenoid
 208 GDGTs (isoGDGTs) and branched GDGTs (brGDGTs) were identified using selected ion
 209 monitoring (SIM) mode based on the detection of the [M+H]⁺ ions, maintaining an integrated
 210 peak area of >2000 and a signal-to-noise ratio of >3 as detection limit. An in-house GDGT
 211 standard was injected ~every 10 samples to trace stability of the system, and provide control on
 212 analytical uncertainty.

213 A set of samples within one interval of low GDGT concentrations (371.035–371.565
 214 mcd) were pooled with neighboring samples to achieve the required amount of GDGTs for
 215 appropriate signal-to-noise ratios, resulting in 11 pooled sample intervals of 2 cm representing
 216 between 2.3 and 9.8 grams of extracted sediment.

217 2.4.2 GDGT-based proxies

218 We reconstructed temperatures using the isoGDGT-based TEX₈₆ paleothermometer
 219 (Equation 1). IsoGDGTs in marine sediments are predominantly produced by shallow-
 220 subsurface-ocean (~50–200 m) dwelling Nitrososphaerales ([Massana et al., 2000](#); [Sinninghe](#)
 221 [Damsté et al., 2002](#); [Schouten et al., 2002](#); [Hurley et al., 2018](#)). However, sedimentary
 222 isoGDGTs potentially contain significant contributions of other sources, e.g., from terrestrial,
 223 deeper-marine, methanotrophic, methanogenic or anaerobic methane oxidizing archaea
 224 communities, which can compromise the TEX₈₆ - temperature relationship ([Hopmans et al.,](#)
 225 [2004](#); [Blaga et al., 2009](#); [Zhang et al., 2011, 2016](#); [Weijers et al., 2011](#); [Taylor et al., 2013](#)).
 226 Therefore, all data were tested for such contributions by several published indices and ratios
 227 using the R-script from [Bijl et al. \(2021\)](#) before further implementation of TEX₈₆
 228 paleothermometry.

229

$$230 \text{TEX}_{86} = \frac{\text{isoGDGT-2} + \text{isoGDGT-3} + \text{cren'}}{\text{isoGDGT-1} + \text{isoGDGT-2} + \text{isoGDGT-3} + \text{cren'}} \quad (1)$$

231

232 TEX₈₆ values were translated to shallow subsurface temperatures at a 100–250 m depth
 233 range (SubT₁₀₀₋₂₅₀), following the calibration by [Ho and Laepple \(2016\)](#) to track the temperature
 234 variability in the niche of Nitrososphaerales in the water column. Importantly, the general one-
 235 to-one covariance of shallow SubTs and SSTs, for instance depicted by models, legitimizes
 236 reconstruction of SST variability through shallow SubT reconstructions ([Ho and Laepple, 2016](#);
 237 [Fokkema et al., 2023](#)). Additionally, we estimated absolute SSTs using the TEX₈₆^H calibration,
 238 which calibrates GDGTs in a global surface sediment dataset to satellite-based surface ocean
 239 temperatures ([Kim et al., 2010](#)). However, because the latitudinal temperature gradient is larger
 240 in the surface ocean than in the shallow subsurface ocean, SST calibrations have larger TEX₈₆-
 241 temperature slopes than SubT calibrations. Consequently, application of TEX₈₆-SST calibrations
 242 expectedly leads to an overestimation of SST variability ([Ho and Laepple, 2016](#)). Importantly,

243 while absolute SSTs remain challenging to accurately reconstruct, here we prioritize the
 244 reconstruction of SST variability. For this, a combined SubT and SST calibration approach gives
 245 a proper lower (SubT₁₀₀₋₂₅₀-calibration) and upper (TEX₈₆^H-SST calibration) estimate of SST
 246 change. Hence, relative SST changes will be reported here as $\Delta\text{SubT}-\Delta\text{SST}$.

247 BrGDGTs are membrane lipids that are generally associated with soil bacteria, but are
 248 also produced in river, or coastal marine environments (Peterse et al., 2009; Zell et al., 2013;
 249 Sinninghe Damsté, 2016). Their abundance relative to that of crenarchaeol, an isoGDGT
 250 exclusively produced by marine Nitrososphaerales is generally used to trace terrestrial organic
 251 matter input into a marine system, and identify possible terrestrial isoGDGT contribution. For
 252 this, we applied the branched and isoprenoid tetraethers (BIT) index (Hopmans et al., 2004)
 253 (Equation 2), where samples with higher values (>0.4 ; Weijers et al., 2006) are customarily
 254 associated with dominant contributions of terrestrial organic matter, and left out of the TEX₈₆
 255 dataset.

256

$$257 \text{ BIT index} = \frac{\text{brGDGT-Ia} + \text{brGDGT-IIa} + \text{brGDGT-IIa'} + \text{brGDGT-IIIa} + \text{brGDGT-IIIa'}}{\text{Cren} + \text{brGDGT-Ia} + \text{brGDGT-IIa} + \text{brGDGT-IIa'} + \text{brGDGT-IIIa} + \text{brGDGT-IIIa'}} \quad (2)$$

258

259 To assess the primary source of brGDGTs, i.e., soil vs marine, we determined the
 260 weighted number of cyclopentane moieties in tetramethylated brGDGTs ($\#rings_{tetra}$) (Equation
 261 3), as brGDGTs produced in the marine realm are characterized by a higher degree of cyclisation
 262 (Peterse et al., 2009; Sinninghe Damsté, 2016). Furthermore, we calculated the ratio of acyclic
 263 hexa- to pentamethylated brGDGTs (IIIa/IIa) (Equation 4), which is positively correlated to
 264 marine *in situ* production of brGDGTs (Xiao et al., 2016). Specifically, in the modern system,
 265 soils typically show IIIa/IIa ratios below 0.59 and marine sediments show ratios above 0.92
 266 (Xiao et al., 2016, 2020). Additionally, we used the total GDGT assemblage (isoGDGTs +
 267 brGDGTs) to infer the depositional setting using the machine learning algorithm "BigMAC"
 268 (Martínez-Sosa et al., 2023), capable of distinguishing marine, lake, peat and soil settings.

269

$$270 \#rings_{tetra} = \frac{\text{brGDGT-Ib} + 2 \times \text{brGDGT-Ic}}{\text{brGDGT-Ia} + \text{brGDGT-Ib} + \text{brGDGT-Ic}} \quad (3)$$

271

$$272 \text{ IIIa/IIa} = \frac{\text{brGDGT-IIIa} + \text{brGDGT-IIIa'}}{\text{brGDGT-IIa} + \text{brGDGT-IIa'}} \quad (4)$$

273

274 The degree of methylation of 5-methyl brGDGTs, which in soils correlates to mean
 275 annual temperatures (Weijers et al., 2007), was calculated using the Methylation of Branched
 276 Tetraethers index (MBT'5me; De Jonge et al., 2014) (Equation 5). For the samples with
 277 presumed soil-dominated brGDGT sources (i.e., BIT index > 0.4) we translated MBT'5me index
 278 values to mean air temperatures for months above freezing (MAF) using the BayMBT₀
 279 calibration (Dearing Crampton-Flood et al., 2020). Roman numerals in all equations refer to
 280 molecular structures in De Jonge et al. (2014).

$$MBT'_{5me} = \frac{brGDGT1a + brGDGT-1b + brGDGT-1c}{brGDGT-1a + brGDGT-1b + brGDGT-1c + brGDGT-11a + brGDGT-11b + brGDGT-11c + brGDGT-111a} \quad (5)$$

283 2.5 Palynology

284 Forty-four samples were prepared for palynological analysis, predominantly concentrated
 285 between 368.9 and 371 mcd. Between 0.84 and 2.09 gram of sample was crushed to ~0.5 cm
 286 chunks and weighed. Next, the sample was transferred to a plastic beaker and one tablet
 287 containing a known amount of *Lycopodium clavatum* spores was added. Any carbonates were
 288 removed by adding 10% HCl and after settling, the liquid was removed by decantation. Next,
 289 silicates were removed by two 40% HF treatments, followed by adding 30% HCl, thereby
 290 decanting the liquids after each step and settling/centrifuging. Finally, the sieved residue between
 291 250 and 10 μm was mounted on microscope slides. Total palynomorphs were counted by
 292 microscope on 400x to 1000x magnification until at least 100 determinable dinocysts were
 293 reached. Count data are combined with previous lower resolution analyses (Sluijs et al., 2009)
 294 after a consistency check, reaching a total dataset of 108 samples across Core 27X.

295 2.6 Spectral analysis

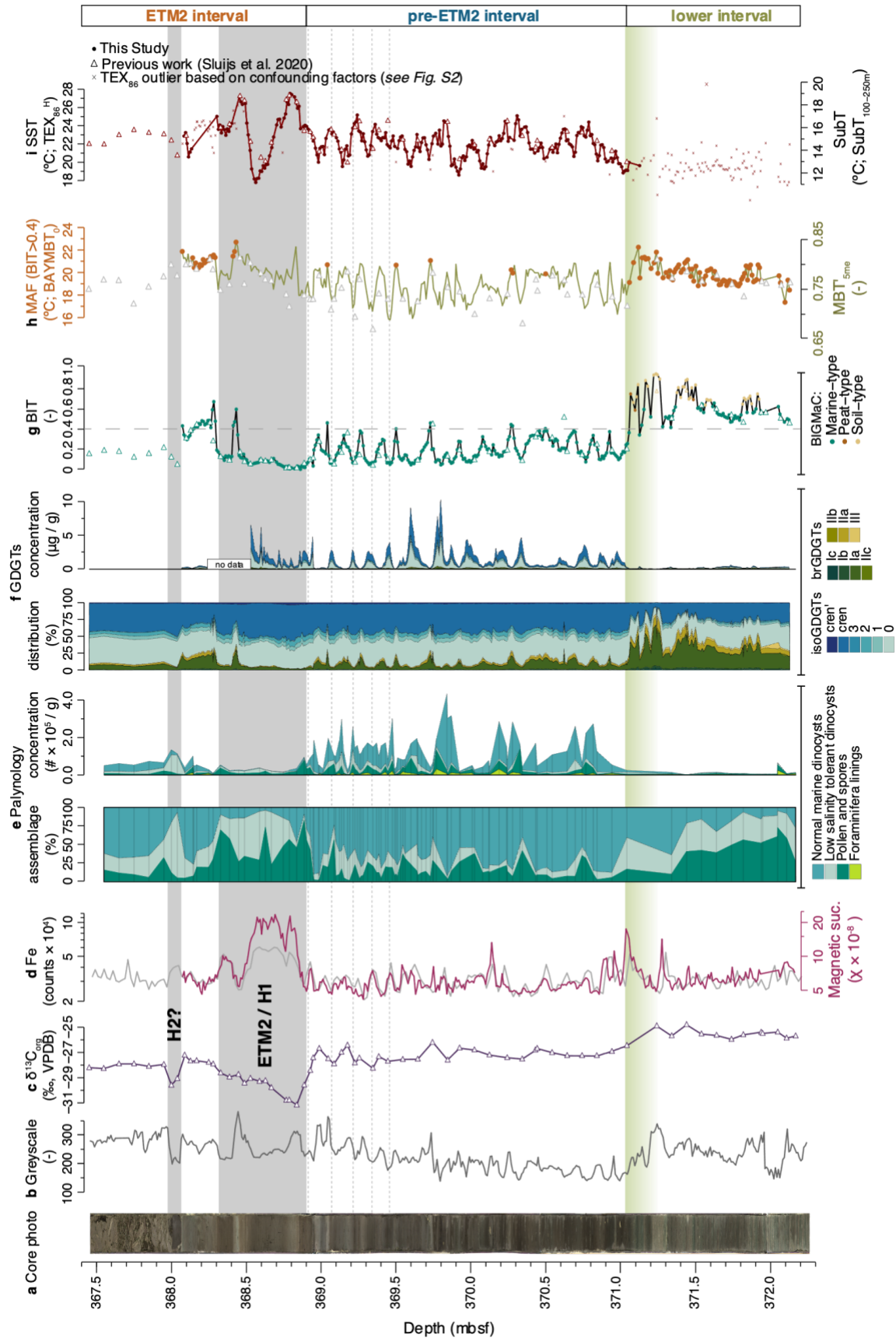
296 To evaluate the presence and amplitude of orbital frequencies in the our generated
 297 records, we performed spectral analysis using Acycle (Li et al., 2019). First, all records were
 298 interpolated on 1 cm and subsequently detrended (LOWESS) to remove background trends.
 299 Power spectra were generated using the Multi-Taper-Method and tested for significance against
 300 90% and 99% confidence intervals of AR(1) noise. Power was translated to (normalized)
 301 amplitude of the signals using a built-in function by Acycle. For bandpass filtering of orbital
 302 components, a bandwidth of ~1/5 of the targeted orbital frequency was used. For phase and
 303 coherence analysis between two signals, the values were taken at the frequencies that
 304 corresponded with the highest coherence within the frequency bands of the targeted orbital
 305 components.

306 3 Results

307 3.1 Sediment characteristics

308 Based on the general sediment characteristics and the position of the ETM2 event (Sluijs
 309 et al., 2009), we divide the analyzed Core into three sections: the ETM2 event interval (368.0–
 310 368.9 mcd), the cyclic pre-ETM2 interval (368.9–371.0 mcd) and the greenish bottom interval
 311 (371.0–372.1 mcd) (see Fig. 3).

312 The MS ranges between $0.4 \times 10^{-8} \chi$ and $2.5 \times 10^{-8} \chi$, with highest values corresponding to
 313 the CIE of ETM2 (Fig. 3d). A gradual decrease in MS values between 372.1–371.0 mcd marks
 314 the bottom interval of the core, ending with a high peak at 371 mcd, on the transition from
 315 greenish to dark grey sediments. High correspondence between the features in the MS and XRF-
 316 based Fe data presented by (Sluijs et al., 2008b) corroborates the general notion that bulk MS
 317 variability traces the relative abundance of Fe-rich, magnetic minerals in the sediments. Hence,
 318 the decimeter scale variations in Fe content, as previously observed in the pre-ETM2 interval
 319 (Sluijs et al., 2008b), are also displayed in the MS record. The cyclic variations within the MS
 320 record generally correspond to alternation of dark and light sediment layers with dark layers (low
 321 greyscale values) corresponding to high MS and vice versa.
 322



324 **Figure 3.** ACEX Core 27X analysis results. **(a)** Core picture. **(b)** Greyscale. **(c)** Total organic
 325 carbon $\delta^{13}\text{C}$ (Sluijs et al., 2009). **(d)** MS and Fe (Sluijs et al., 2008b). **(e)** Palynology, with
 326 relative abundances of cysts of normal marine, and freshwater tolerant dinoflagellates and pollen
 327 and spores, and concentrations of palynomorphs per gram of dry sediment. **(f)** GDGTs, with
 328 relative abundances (%) and absolute concentrations (ng/g of dry weight sediment) of all
 329 GDGTs. **(g)** BIT index, in which colors of datapoints mark the depositional environment
 330 indicated by the BIGMaC machine learning algorithm based on total GDGT distributions
 331 (Martínez-Sosa et al., 2023). **(h)** MBT'5_{me} values, where green points mark datapoints with BIT
 332 > 0.4, which can be translated to MAF (top axis)). **(i)** TEX₈₆-based SST (bottom axis) and SubT
 333 (top axis). Triangles mark data previously generated by (Sluijs et al., 2020), small crosses mark
 334 TEX₈₆ data influenced by non-thermal factors based on the indices and ratios in Supporting Fig.
 335 S2. Grey bars mark hyperthermal events ETM2 and H2, green bar marks a presumed condensed
 336 interval.
 337

338 3.2 Palynological assemblages

339 Palynomorph assemblages consist predominantly of reasonably to well preserved pollen,
 340 spores, and aquatic palynomorphs, typically marine and low-salinity tolerant dinocysts, with
 341 locally abundant leiosphaerids (a group of aquatic palynomorphs of unknown affinity).
 342 Occasional poor preservation of notably dinocysts causes seven samples too poorly preserved for
 343 dinocyst assemblage quantification. The long-term trends, as previously reported by Sluijs et al.
 344 (2009), depict high abundances of terrestrial palynomorphs and Peridinioid dinocysts with
 345 hexagonal 2a archeopyles – considered to have been produced by low-salinity-tolerant
 346 dinoflagellates (e.g., [Sluijs and Brinkhuis, 2009](#); [Frieling and Sluijs, 2018](#)) – within the bottom
 347 interval and ETM2 (Fig. 3e). The pre-ETM2 interval is marked by considerably lower, but
 348 variable concentrations of terrestrial palynomorphs and low-salinity tolerant dinocysts, showing
 349 variations of approximately 0–40 % and 5–50 %, respectively, and much higher abundances of
 350 species that reflect typical shelf conditions, also consistent with the previous lower resolution
 351 work (Sluijs et al., 2009). The concentrations of dinocysts (Fig. 3e) vary between ~1,200 and
 352 550,000 specimens per gram of sediment, with highest concentrations in the pre-ETM2 interval
 353 and lowest concentrations in the interval below 371 mcd. Organic linings of benthic foraminifera
 354 are present as well, sporadically. Foraminifer linings are mainly concentrated in the pre-ETM2
 355 interval and absent in ETM2 itself.

356 3.3 GDGTs

357 3.3.1 GDGT relative abundances and concentrations

358 Sediments are generally rich in GDGTs with concentrations ranging between 3 and
 359 10,000 ng/g, with highest abundances at 369.755 and 369.555 mcd (Fig. 3f). For 42 samples
 360 (368.035–368.505 mcd) GDGT concentrations could not be determined as they were injected
 361 without the GDGT standard. At least one of the isoGDGTs was below the detection limit in 13
 362 out of 372 analyzed samples, which were therefore left out of subsequent analyses.

363 The total GDGT concentrations exhibit clear variability in the pre-ETM2 interval, at the
 364 same decimeter-scale as the other records (i.e., greyscale, MS, Fe, terrestrial palynomorphs),
 365 with highest total GDGT concentrations in dark, organic and iron-rich layers (Supp. Fig. S1).
 366 Total GDGT concentrations are low in the lower interval, with a minimum around 371.0–371. 2

367 mcd and exhibit low variability. Concentrations of brGDGTs are generally lower than the
368 isoGDGTs, except for a few samples in the lower interval, and range between 0.16–500 ng/g and
369 0.13–187 ng/g, respectively. Within ETM2, isoGDGTs dominate the total GDGT distributions.
370 The concentrations of brGDGTs closely covary with that of the isoGDGTs in the pre-ETM2
371 interval. However, the relative proportion of brGDGTs increases during the light-colored
372 intervals (with low total GDGT concentrations) and vice versa.

373 3.2.2 GDGT distributions

374 All samples with isoGDGTs above detection limit ($n = 359$) were screened for potential
375 confounding factors on the TEX_{86} using a set of GDGT ratios and indices established in the
376 literature (Supp. Fig. S2). Specifically, as noticed during the previous low-resolution analyses of
377 Core 27X (Sluijs et al., 2020), the GDGT-2/GDGT-3 ratio is high in the interval leading up to
378 ETM2, reaching up to 13.8, pointing to a clearly dominant GDGT sourcing below the surface
379 mixed layer. Here, we keep all data with GDGT-2/GDGT-3 ratio >5 in the dataset, but interpret
380 it as evidence for isoGDGT contributions from below 200 m (e.g., Hurley et al., 2018). The other
381 isoGDGT indices are predominantly below their defined cut-off values, except for the enigmatic
382 second half of ETM2 (~368 – 368.5), which is marked by high values for the methane index,
383 AOM index, methanogenesis and ΔRI (Supp. Fig. S2), implying that the TEX_{86} - temperature
384 relationship is presumably compromised there because of significant isoGDGT contributions
385 from different archaeal communities.

386 The $\#ring_{\text{Tetra}}$ is overall low throughout the complete record (<0.25). Assuming that
387 values >0.7 indicate a marine origin in the modern system (Sinninghe Damsté, 2016), this
388 suggests a dominant terrestrial brGDGT source, consistent with previous ACEX records (Willard
389 et al., 2019; Sluijs et al., 2020). A dominant terrestrial brGDGT sourcing is consistent with the
390 IIIa/IIa ratios, which average 0.51, 0.53 and 0.32 for the ETM2, pre ETM2 and lower intervals,
391 respectively (Supp. Fig. S3).

392 The BIT index is generally highest in the lower interval (mean = 0.61) and above 368.26
393 mcd (mean = 0.43), while lowest values are within ETM2 (mean = 0.12). In the pre-ETM2
394 interval the BIT index regularly varies between 0.06 and 0.51 on decimeter scale (mean = 0.21).
395 Particularly in the lower interval, BIT index values are above the general cut-off of 0.4 that is
396 used to identify a pronounced impact of soil-derived isoGDGTs on TEX_{86} paleothermometry (n
397 = 122) (Fig. 3g, Supp. Fig. S2).

398 The BIGMaC algorithm indicates a dominant marine depositional environment based on
399 the distribution of the total GDGT pool in the studied interval (Fig. 3g), including 84 samples
400 where more terrestrial input is expected based on higher (>0.4) BIT index values. Samples that
401 BIGMaC classifies as dominantly terrestrial (either peat- or soil-sourced) exclusively occur in
402 the lower interval, characterized by $\text{BIT} > 0.58$ and $\#ring_{\text{Tetra}} < 0.16$.

403 3.3.3 Temperature reconstructions

404 We translate the isoGDGT distributions into SubTs of ~11–19 °C following the SubT_{100-}
405 $_{250\text{m}}$ calibration. This corresponds to SSTs of ~18–27 °C using the $\text{TEX}_{86}^{\text{H}}$ calibration (Kim et al.,
406 2010) (Fig. 3i). Peak temperatures are reached during the ETM2 event, marked by a warming
407 from background SubTs of 13–16 °C (SSTs = 20–24 °C) to peak temperatures of 19 °C (SST =
408 27 °C), signifying an averaged warming of 4.5–5.5 °C ($\Delta\text{SubT} - \Delta\text{SST}$). Apart from the two
409 apparent maxima in the TEX_{86} record related to ETM2 (368.4 and 368.75 mcd), we identify four

410 earlier local SST maxima that occur in intervals of approximately 50 cm: at ~369.25, 369.75,
 411 370.25 and 370.75, with peak SubTs of ~17 °C (SSTs= ~24–25 °C). In the pre-ETM2 interval,
 412 the SST record also exhibits smaller, decimeter scale cyclic variations, depicting a total
 413 variability up to 3–5 °C ($\Delta\text{SubT}-\Delta\text{SST}$).

414 The analytical error in the TEX_{86} , determined by the standard deviation of 62
 415 measurements of the in-house GDGT standard, is 0.005 TEX_{86} units. In the TEX_{86} range of the
 416 early Eocene Arctic, this analytical error amounts to 0.20 °C for SubTs and 0.26 °C for SSTs.
 417 Although this uncertainty does not include any potential errors associated with extraction and
 418 fractionation, the low analytical error implies high confidence on the reconstructed direction and
 419 magnitude of SST variability, which is the prime goal for this study.

420 Decimeter-scale variations within the $\text{MBT}'_{5\text{me}}$ record display a high correspondence with
 421 the BIT index, where low BIT index values correspond with the lower $\text{MBT}'_{5\text{me}}$ values and *vice*
 422 *versa*. For the samples with BIT > 0.4 (n = 122), we converted $\text{MBT}'_{5\text{me}}$ to MAF, resulting in
 423 mean temperatures of 20 °C, and a warming of ~2 °C to peak temperatures of ~23 °C associated
 424 with the ETM2 (Fig. 3h). A second MAF peak is recorded at ~371.2 mbsf, reaching ~22 °C. In
 425 comparison with the previously published low-resolution data generated on the same instrument
 426 in 2018, the BIT values are well in agreement (Sluijs et al., 2020), whereas the $\text{MBT}'_{5\text{me}}$ values
 427 are overall slightly (~0.02) higher (Willard et al., 2019).

428

429 **4 Spectral analysis and tuning**

430 4.1 Spectral analysis of pre-ETM2 interval

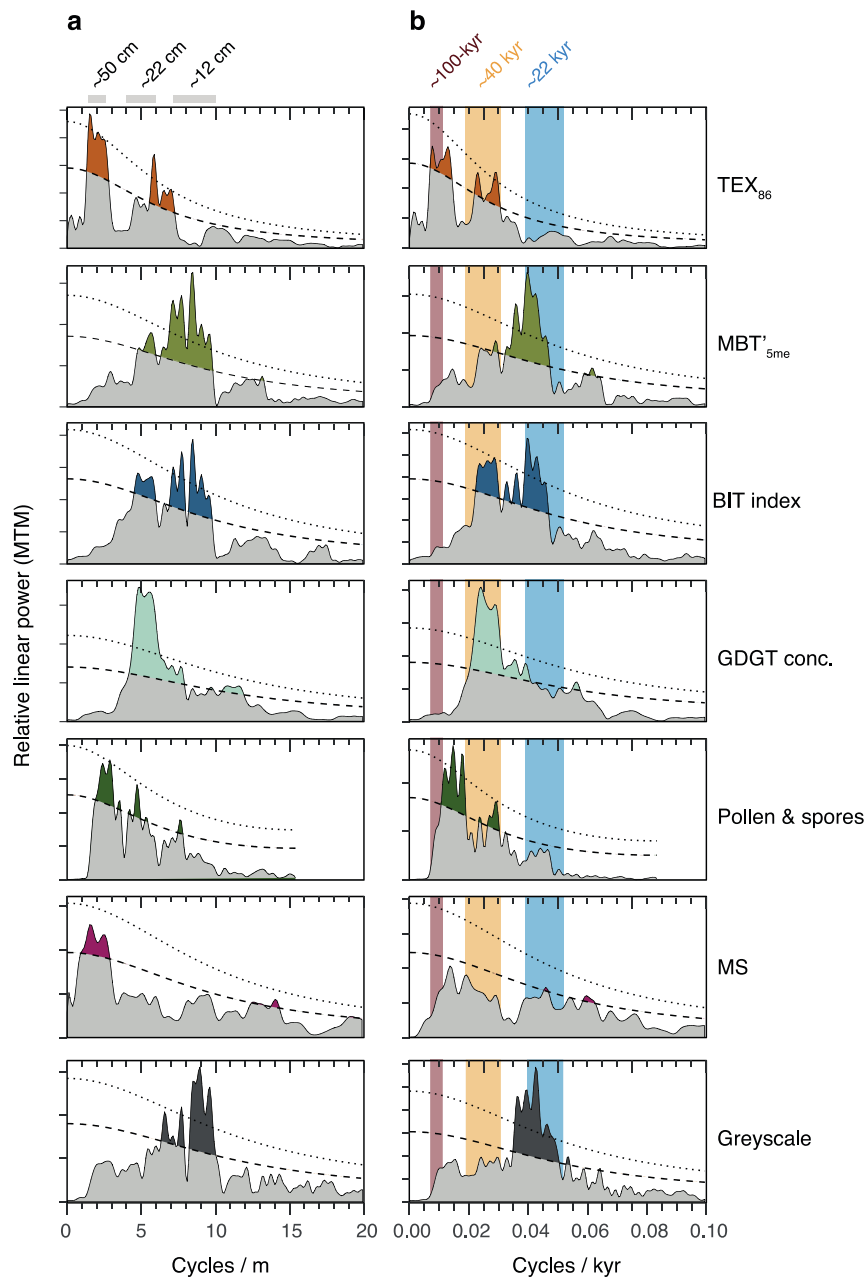
431 The suite of environmental proxy data (Fig. 3) shows a concentration of apparently cyclic
 432 variability in the pre-ETM2 interval of 368.9–371.0 mcd, comprising the most distal marine
 433 sequence according to our data, characterized by generally low relative proportions of terrestrial
 434 palynomorphs, low BIT index values, and low MS values. Therefore, to analyze the imprint of
 435 orbital cycles on Arctic (hydro)climate variability, we focus on the pre-ETM2 interval for
 436 spectral analysis, thereby excluding ETM2 itself and the lower interval.

437 The MTM power spectra (Fig. 4a) show that the observed regular decimeter-scale
 438 variability in the generated records in the pre-ETM2 interval are expressed as significant spectral
 439 components for nearly all datasets generated in this study. The analyzed datasets exhibit
 440 dominant frequencies of 1.5–2.5 cycles / m (mainly TEX_{86} , but also MS; pollen/spores), 4–6
 441 cycles / m (GDGT concentrations; BIT index; $\text{MBT}'_{5\text{me}}$ index; TEX_{86} ; pollen and spores) and 8–
 442 10 cycles / m (BIT index; $\text{MBT}'_{5\text{me}}$ index; greyscale), representative of periodicities of
 443 approximately 50, 22 and 10–14 cm, respectively. The ratio between the predominant 50, 22,
 444 10–14 cm periodicities approximates the ratio between ~100-kyr eccentricity, 41-kyr obliquity
 445 and 22-kyr precession. This hypothesis is substantiated by a close relation between the amplitude
 446 modulation of the 10–14 cm precession related cycles (e.g., in greyscale and total GDGT
 447 concentration) by ~50 cm eccentricity cycles (i.e., in TEX_{86}) (**Fig. 5**). Spectral analysis of the
 448 XRF-based Fe record across a much larger interval (Cores 29X–27X; Sluijs et al., 2008b), found
 449 slightly lower frequencies, but consistent ratios indicating the same orbital forcing.
 450 Consequently, following above cyclostratigraphic interpretation, sedimentation rate in the here-
 451 studied interval was ~0.5 cm / kyr, which compares well to the 0.6–0.7 cm / kyr based on
 452 chemostratigraphic constraints for the larger interval (Sluijs et al., 2008). The slight offset could

453 relate to a reduced siliciclastic sediment input during this interval, because the pre-ETM2
 454 interval covers the most distally marine depositional setting of the analyzed sections by Sluijs et
 455 al. (2008).

456 We tune our record to the astronomical solution based on the solid, orbitally tuned, age
 457 constraint of the ETM2 event starting at 54.005 Ma, and the clear expression of the ~100-kyr
 458 eccentricity cycles in the TEX_{86} record, of which the phase relation is deduced from its
 459 amplitude modulation of precession in several other records (**Fig. 5**). We identify four 100-kyr
 460 eccentricity maxima, which we tune to the maxima of 54.15, 54.25, 54.35 and 54.45 Ma of the
 461 La10b eccentricity solution (Laskar et al., 2011).

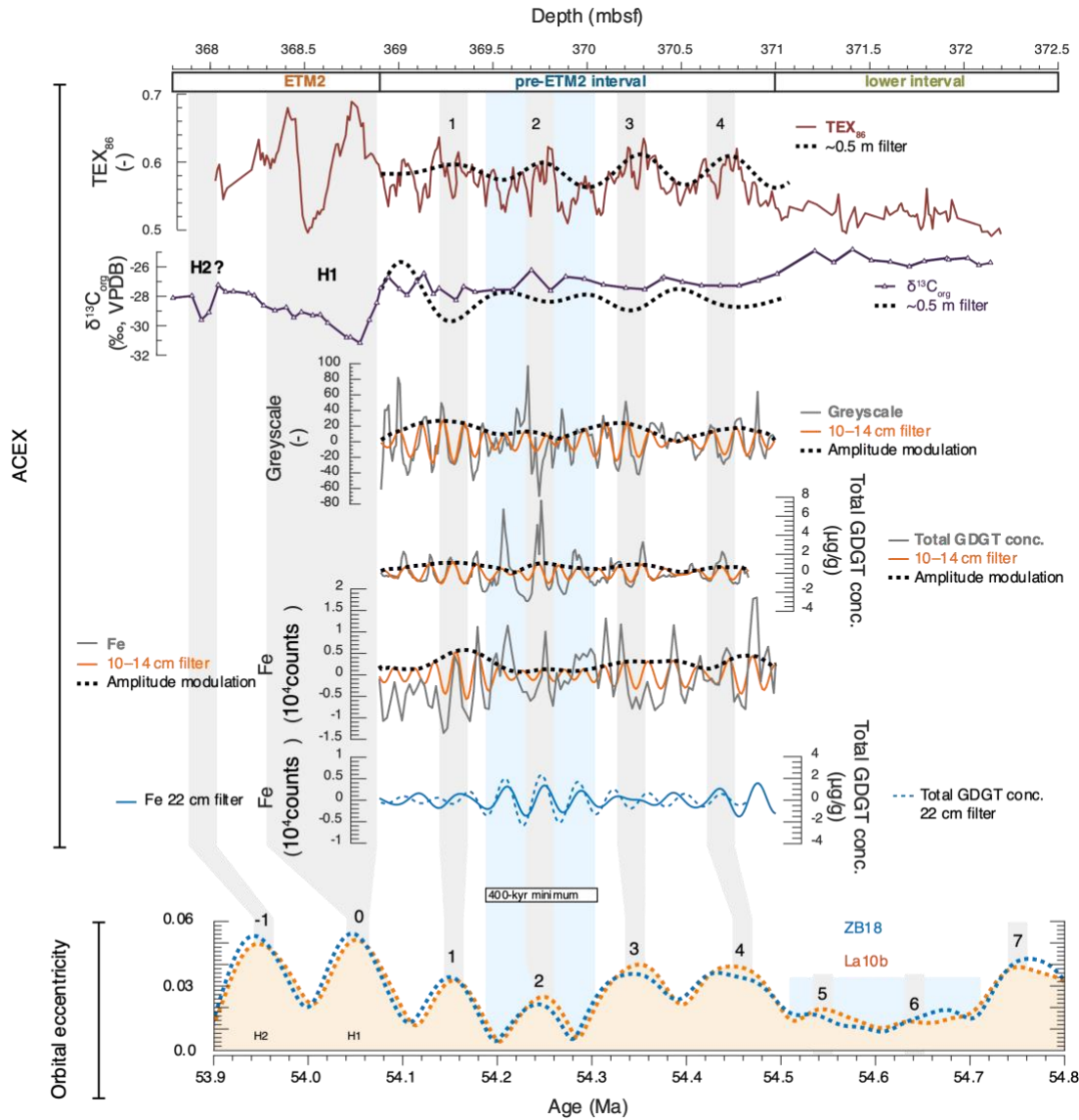
462



463

464 **Figure 4.** MTM Power spectra in depth (a) and age (b) domains. Dashed and dotted lines
 465 indicate 90% and 99% confidence intervals of AR(1), respectively.

466



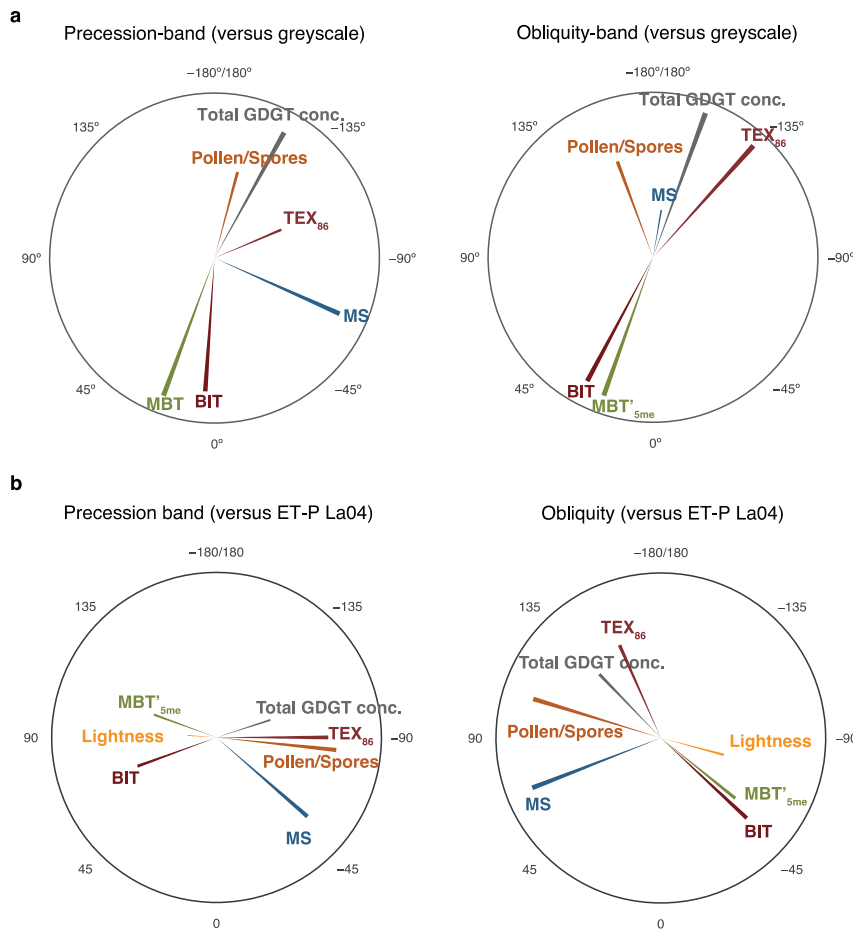
467 **Figure 5.** Tuning of the pre-ETM2 interval of ACEX to eccentricity. Eccentricity maxima are numbered relative to
 468 the ETM2 related maximum.
 469

470

471 After tuning, spectral analysis in the age domain (Fig. 4b) indicates that BIT, MBT'_{5me},
 472 greyscale and MS exhibit dominant periodicities in the precession band, whereas TEX₈₆ and total
 473 GDGT concentrations exhibit dominant obliquity frequencies. Records of terrestrial
 474 palynomorphs have less clearly pronounced forcing by the identified astronomical cycles, likely
 475 due to the lower sample resolution than the other proxy records, but a modest signal of obliquity
 476 is present. The imprint of short eccentricity is most clearly expressed in the power spectrum of

477 TEX_{86} . Interestingly, a dominant ~ 17 cm periodicity of the TEX_{86} record amounts to ~ 33 kyr
 478 following our tuning. Indeed, obliquity has a ~ 30 kyr component (Fig. 2) derived from the
 479 secular resonance of $p + s_2$. However, this is only a minor component compared to the dominant
 480 obliquity of ~ 41 kyr. A significant periodicity of ~ 30 kyr in Pleistocene records is typically
 481 ascribed to a combination tone (e.g., Lourens et al., 2010), such as short eccentricity and
 482 obliquity ($1/100 + 1/41 = 1/29$), double obliquity and single obliquity ($1/82 + 1/41 = 1/27$) or 19-
 483 kyr precession and obliquity ($1/19 - 1/41 = 1/35$). As this frequency is only dominantly present in
 484 the TEX_{86} record, which shows significant forcing by short eccentricity and obliquity, we
 485 presume that this ~ 30 kyr cycle is a combination tone of the 100-kyr eccentricity and 41-kyr
 486 obliquity cycles.

487



488

489 **Figure 6.** Phasing of proxy records in precession and obliquity bands. Phases are plotted as
 490 degree difference to the sediment greyscale record (a) and to ETP (negative precession) of La04
 491 (b). Length of the bars indicate correspondence.

492

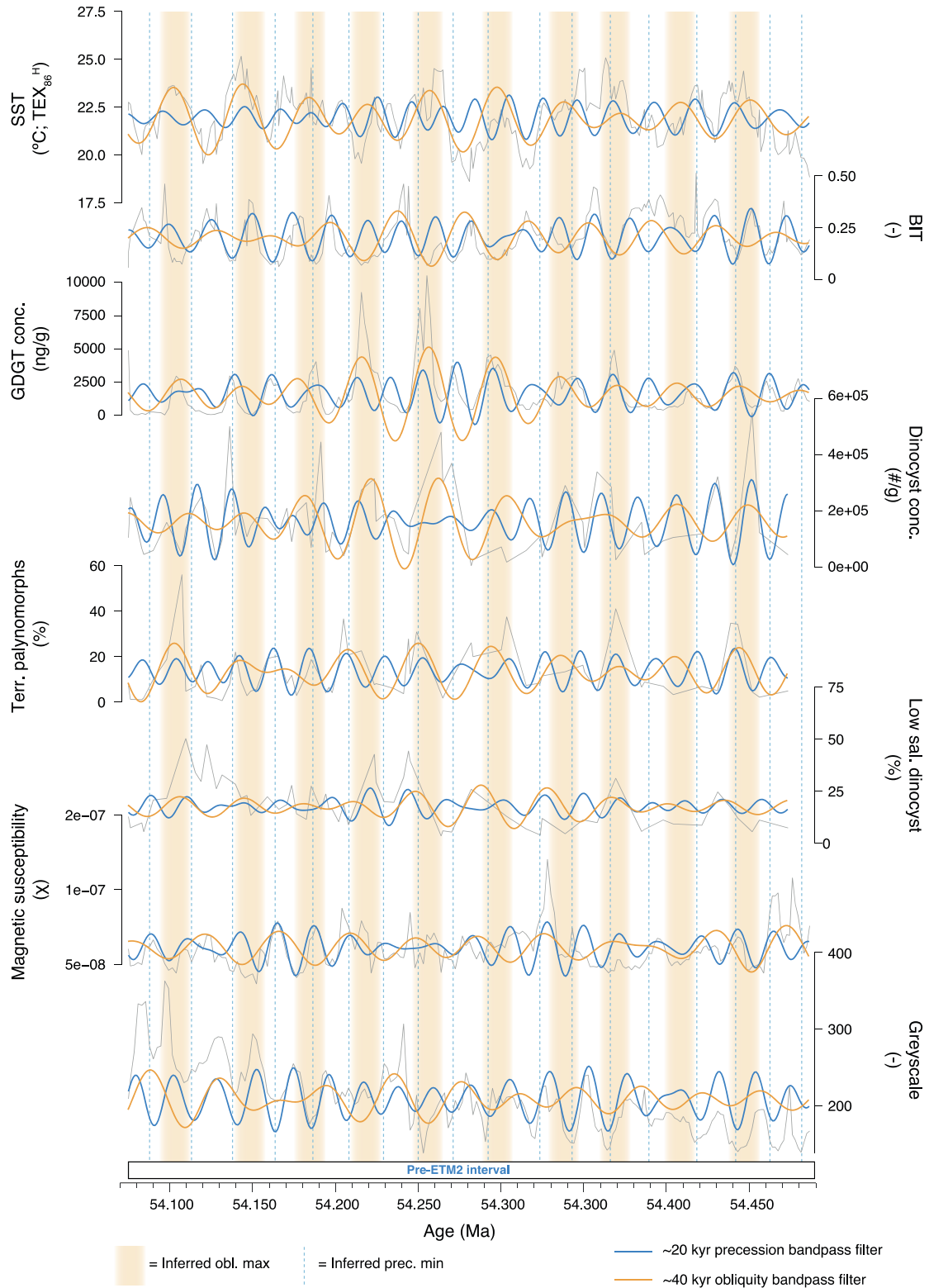


Figure 7. Tuned paleoenvironmental proxy data across the pre-ETM2 interval of ACEX and bandpass filters for precession (a) and obliquity (b). Orange bars mark inferred obliquity maxima; blue dotted lines mark inferred precession minima.

497 4.2 Amplitude and phasing

498 The correspondence and phasing of the precession and obliquity signals were calculated
499 relative to the sediment color and to the orbital solution (Fig. 6). Note that the precession and
500 obliquity components of the orbital solution are subject to uncertainty in the early Eocene, due to
501 chaotic behavior in the solar system (Laskar et al., 2004; Zeebe and Lourens, 2019), and their
502 respective phasing is not considered in absolute sense. Nevertheless, they provide a steady and
503 independent rhythm for comparison between the other proxy-derived components. On both
504 precession and obliquity timescales there is a correspondence between the BIT index, MBT'_{5me}
505 index, and greyscale, in antiphase with TEX₈₆, total GDGT concentrations, and terrestrial
506 palynomorphs (Figs. 6, 7). MS is approximately in phase with the TEX₈₆, terrestrial
507 palynomorph abundances, and total GDGT concentrations, but shows a conspicuous general lead
508 (or lag) with respect to the other records. Remarkably, temperature proxies TEX₈₆ and the
509 MBT'_{5me} index are in near antiphase across the orbitally driven variations in the pre-ETM2
510 interval. Similarly, terrestrial palynomorph abundances and the BIT index, both indicators for
511 terrestrial input, are in antiphase for most of the record.

512 For multiple records (including Fe and total GDGT conc. (Figs. 5, 7), highest imprint of
513 obliquity cycles (and reduced imprint of precession) is concentrated between 54.180 and 54.320
514 Ma, coinciding with a 400-kyr eccentricity minimum. The correspondence between long-term
515 eccentricity nodes and the emergence of obliquity in paleoclimate signals has been observed for
516 other intervals and locations (e.g., [Westerhold et al., 2014](#)).

517

518 5 Discussion

519 5.1 Relative sea level change

520 The sediments of the lower interval (<371 mcd) are likely deposited in a proximal marine
521 setting, just below wave base. This is evidenced by the high BIT index values, peat/soil-derived
522 GDGT distributions assigned by the BigMAC algorithm, high proportions of terrestrial
523 palynomorphs, high proportions of low-salinity-dominant dinocysts, low abundance of normal
524 marine dinocysts, and low GDGT-2/GDGT-3 ratios. Contrastingly, the pre-ETM2 interval is
525 characterized by a more offshore marine depositional setting, evidenced by low BIT index
526 values, marine-associated GDGT distributions, low proportions of terrestrial palynomorphs, high
527 GDGT-2/GDGT-3 ratios, and dominance of normal marine dinocysts. Specifically, one critical
528 observation for a deeper environmental setting in the pre-ETM2 interval are the high GDGT-
529 2/GDGT-3 values in the preETM2 interval (mean = 7.8 (SD=2.2); Supp. Fig. S2). In the modern,
530 marine sedimentary GDGT-2/GDGT-3 ratios below 5 indicate an isoGDGT export depth from
531 maximally 150 – 200 m water depth, but ratio values rapidly increase with GDGT contributions
532 from deeper waters because of contributions of a distinct deeper dwelling Nitrososphaerales
533 clade (Taylor et al., 2013; Hurley et al., 2018; van der Weijst et al., 2022; Rattanasriampaipong
534 et al., 2022). Crucially, GDGT assemblages with GDGT-2/GDGT-3 ratios exceeding 5 are rarely
535 produced shallower than 200 m depth (Taylor et al., 2013; Hurley et al., 2018). While we
536 acknowledge that the non-analogue situation of the Eocene Arctic might have led to anomalous
537 GDGT ratios, GDGT-2/GDGT-3 ratios averaging 7.8 strongly suggest that the paleodepth
538 reached deeper than 200 m during the pre-ETM2 interval.

539 The boundary between the lower and pre-ETM2 interval (~371.0 – 371.2 mcd; dated at
 540 ~54.55 Ma) is characterized by an organic-lean interval of numerous multi-cm-scale green
 541 layers, presumably rich in glauconite (Sluijs et al., 2020). We surmise that this interval marks a
 542 condensed section that spans the onset of a transgression, when increasing landward
 543 accommodation space reduces the sedimentation on the distal shelf. The magnitude of relative
 544 sea level change across this interval was presumably at least 100 m, if the lower interval was
 545 deposited close to wave base and the pre-ETM2 interval was deposited at water depths exceeding
 546 200 m. Therefore, this sea level rise was likely initiated by a phase of (cooling induced)
 547 subsidence of the Lomonosov Ridge around 54.55 Ma, following its Paleocene rifting. Given
 548 some evidence of potentially coeval transgressive surfaces in the North Sea (Powell et al., 1996)
 549 and New Jersey (sequence E1 of Browning et al. (1996)), some effect of eustasy cannot be
 550 excluded (Sluijs et al., 2008a). However, given the absence of large ice sheets during this time
 551 interval, the relative contribution of eustatic rise would be negligible considering the large
 552 magnitude of sea level rise recorded at Lomonosov Ridge. The return to dominant low-salinity-
 553 tolerant dinocysts in younger strata above Core 27X — for which the exact depth and age is
 554 poorly constrained due to the lack of sediment recovery between the top of Core 27X at 367.4
 555 mcd and the bottom of Core 23X at ~345 mcd, but presumably in the Early Eocene Climatic
 556 Optimum (Sluijs et al., 2008b) — suggests that Lomonosov Ridge was uplifted again to resume
 557 very proximal marine sedimentation at the drill site.

558 5.2 Orbitally forced GDGT sourcing in the pre-ETM2 interval

559 5.2.1 Terrestrially versus marine-sourced brGDGTs

560 Curiously, in the relatively distal and deep marine pre-ETM2 interval, variations in BIT
 561 index values negatively correlate to brGDGT concentrations and terrestrial palynomorph
 562 abundances on precession and obliquity timescales (**Figs 3, 6, 7**). Minima in the BIT index
 563 counterintuitively coincide with maxima in brGDGT concentrations, but also even higher
 564 maxima in concentrations of marine isoGDGT crenarchaeol. Given that the orbital age model
 565 excludes changes in siliciclastic sediment supply sufficient to dilute and concentrate GDGTs
 566 across orbital cycles, this strongly suggests that marine productivity of isoGDGTs during these
 567 periods outcompeted the additional terrestrial supply of brGDGTs, hence lowering the BIT
 568 index. We infer that the most likely mechanism behind this phasing is that periodically enhanced
 569 terrestrial nutrient supply due to hydrological and temperature change triggered marine
 570 productivity of both isoGDGTs and brGDGTs on the shelf. Indeed, elevated marine productivity
 571 coinciding with intervals of peak GDGTs is supported by the overall higher organic content in
 572 these (predominantly darker; **Fig. 3**) sediment layers, albeit based on few TOC% measurements
 573 by Sluijs et al. (2008b) (**Supp. Fig. S1**).

574 A significant contribution of in-situ marine produced brGDGTs is on first sight
 575 contrasted by overall low #rings_{Tetra} values throughout the record (<0.25), i.e., values generally
 576 associated with a primarily soil-derived brGDGT origin. However, the negative correlation with
 577 the BIT index, reminiscent of modern shelf transects (Sinninghe Damsté, 2016) (**Supp. Fig. S4**),
 578 suggests a degree of covariance between shifts in terrestrial versus marine brGDGT sourcing and
 579 the BIT index. This relationship is further evidenced by the negative relationship between the
 580 BIT index and the brGDGT IIIa/IIa ratio (**Supp. Fig. S3**). Collectively, particularly considering
 581 the antiphase behavior of BIT index values and terrestrial palynomorph abundances, we interpret
 582 that in the pre-ETM2 interval, the BIT index specifically traces the relative contribution of soil-

583 derived brGDGTs to the total brGDGT pool, while the terrestrial palynomorph abundances track
584 the absolute terrestrial input.

585 5.2.2 Shallow versus deep sourced isoGDGTs

586 Exclusively temperature-controlled distributions of isoGDGTs would result in a negative
587 relation between TEX_{86} and GDGT-2/GDGT-3 ratios, simply because Nitrososphaerales increase
588 the number of cyclopentane rings with increasing temperature to maintain membrane rigidity
589 (e.g., Schouten et al., 2002; Rattanasriampaipong et al., 2022). However, similar to the modern
590 ocean surface sediments (Taylor et al., 2013; Rattanasriampaipong et al., 2022) and many
591 downcore records (e.g., van der Weijst et al., 2022), the GDGT2/GDGT3 ratio weakly positively
592 correlates with TEX_{86} in the studied section ($R^2 = 0.25$; Supp. Fig. S5a). In the modern system,
593 this feature has been linked to increased contribution by deeper-dwelling (below pycnocline)
594 GDGT-producers (Rattanasriampaipong et al., 2022). Within the pre-ETM2 interval, the
595 fluctuations of the GDGT-2/GDGT-3 ratio strongly covary with the obliquity and precession
596 scale variations recorded in TEX_{86} . This suggests varying proportional contributions of deeper
597 and shallow living GDGT-producers on orbital timescales.

598 In the absence of significant early Eocene ice sheets, it is unlikely that orbitally forced
599 relative sea level variability was responsible for the observed fluctuations in GDGT-2/GDGT-3.
600 Therefore, we postulate the recorded GDGT-2/GDGT-3 fluctuations to reflect orbitally forced
601 changes in water column structure, for instance through vertical movement of the nitracline
602 depth, periodically allowing for increased GDGT contributions of a deeper dwelling community.
603 The strong negative correlation between GDGT-2/GDGT-3 and BIT index ($R^2 = 0.51$; Supp. Fig.
604 S5b) suggests that these water column fluctuations are coeval with marine productivity changes
605 (see 5.2.1).

606 Importantly, such contributions of deeper dwelling communities do not necessarily
607 impair the TEX_{86} -temperature relationship, as there is no primary control of GDGT-2/GDGT-3
608 ratios on the TEX_{86} (see Equation 1). Suspended particulate matter from >200 m water depth
609 typically has GDGT-2/GDGT-3 ratios >20 (Hurley et al., 2018), and this likely includes GDGTs
610 exported from shallow waters, suggesting that deep dwelling communities produce GDGTs in
611 much higher GDGT-2/GDGT-3 ratios. Average GDGT-2/GDGT-3 ratios of 7.8 therefore only
612 indicate relatively modest GDGT contributions from deeper waters. This is further supported by
613 reconstructions from the Chilean and Angolan margins, where sets of neighboring sites with
614 substantially different water depths and GDGT-2/GDGT-3 ratios, yield very comparable TEX_{86}
615 records (Varma et al., 2023).

616 5.3 Orbital climate variability of the early Eocene Arctic

617 5.3.1 Temperature

618 Our spectral analyses support the notion that the decimeter-scale variability across the
619 ACEX pre-ETM2 record, as captured in the TEX_{86} record, is associated with orbital cyclicity
620 (Figs. 4, 7). The orbital-scale variation of SST has a strong imprint of obliquity and eccentricity
621 (Fig. 4), with the TEX_{86} MTM spectrum indicating amplitudes of 0.5–0.7 °C and 0.7–0.8 °C,
622 respectively (Supp. Fig. S6). Variability in the precession band, visible as a small peak in the
623 MTM spectrum of TEX_{86} , but below 0.9 AR(1), only has a limited amplitude of ~0.2–0.3 °C.
624 Note that the analytical uncertainty has minimal effect on the reconstructed spectral amplitudes,

625 as this error is normally distributed around the targeted signals. Crucially, the completeness of
626 the cyclicity of the reconstructed SST signal indicates that the complete orbital imprint of SST
627 was reconstructed, demonstrating that there is no bias to one end of the orbital cycle in the
628 sedimentary record of the early Eocene Lomonosov Ridge.

629 In lack of independent data on orbital phasing of the precession and obliquity signals and
630 other driving mechanisms (e.g., the role of atmospheric heat transport), we interpret the SST
631 maxima as insolation maxima at 78°N. Without a-priori knowledge on seasonality of forcing,
632 insolation maxima at a latitude of 78°N correspond to obliquity maxima (Fig. 9), and, if biased
633 towards summer, to precession minima (Fig. 2).

634 The MBT'_{5me} record displays a clear influence of orbital cyclicity as well (Fig. 4). The
635 antiphase of the orbital signals between MBT'_{5me} and TEX₈₆ in the pre-ETM2 interval (Fig. 6)
636 corroborates the inferred changes in terrestrial vs marine-sourced brGDGTs (*see 5.2.1*), because
637 it is virtually impossible that continental air temperature varies oppositely of near-shore SSTs.
638 Therefore, we interpret the orbital variation captured in the MBT'_{5me} record to signify variability
639 in brGDGT sourcing, rather than MAF variability. Interestingly, the MAF reconstructed from
640 samples with BIT > 0.4, which we deem to contain mostly soil-dominated brGDGTs, is
641 approximately ~20–21 °C in the pre-ETM2 interval (calibration error = 3.8 °C (Dearing
642 Crampton-Flood et al., 2020)), and approximately compatible with the minima in TEX₈₆^H-based
643 SSTs (**Fig. 3**), and pollen derived estimates from this interval (Willard et al., 2019). Furthermore,
644 based on these samples, we reconstruct a MAF increase during the peak ETM2 interval of ~2 °C,
645 reaching a maximum of 22.7 °C at 368.3 mcd.

646 5.3.2 Hydrology and marine productivity

647 Cyclic variability in the supply of terrestrial palynomorphs to the Arctic Basin suggests
648 an orbital control on Arctic hydrology in the early Eocene, fitting records of the middle Eocene
649 (Sangiorgi et al., 2008; Barke et al., 2011). Furthermore, indicators for marine productivity (i.e.,
650 total GDGT concentration, TOC content, in the absence of strong changes in sediment
651 accumulation rates) all peak during maxima of terrestrial palynomorphs, suggesting a strong
652 increase in terrestrial nutrient supply to the basin on orbital timescales, presumably through
653 increased runoff (*see 5.2.1*). This signal is in line with the cyclic shift in brGDGT sourcing from
654 marine in-situ dominated (i.e., low BIT) during the phases of high runoff, and terrestrially
655 dominated (i.e., high BIT) during the phases of low runoff.

656 The orbital imprint on early Eocene Arctic temperature and hydrology was likely forced
657 by a combination of variable regional moisture circulation and variable poleward (heat and)
658 moisture transport. Interestingly, the phasing of these two processes is opposite on obliquity
659 timescales: obliquity maxima result in maximum high-latitude summer insolation, and
660 consequently higher evaporation/precipitation rates, whereas obliquity minima result in an
661 enhanced meridional insolation gradient on the summer hemisphere (e.g., Raymo and
662 Nisancioglu, 2003), and consequently an intensified poleward moisture transport (Loutre et al.,
663 2004). If poleward moisture transport was the dominant process causing the hydrological
664 variability, precipitation maxima would occur during obliquity minima. In contrast, we find an
665 in-phase relationship between runoff indicators and TEX₈₆ on both obliquity and precession
666 timescales (**Figs. 6, 7**), which implies that the runoff was in-phase with temperature, and
667 presumably also with insolation.

668 While we acknowledge the lack of independent constraints on the phase relation between
669 our records and astronomical cycles, the positive temperature-runoff phasing strongly suggests
670 that the orbital variation of poleward moisture transport originating from the (sub)tropics was
671 subordinate to that of the regional, high-latitude, hydrological processes. Collectively, this
672 implies that orbitally forced insolation maxima (e.g., obliquity maxima and/or precession minima
673 modulated by eccentricity) caused warmer and more humid conditions in the Arctic region, and
674 this was expressed by increased regional evaporation, precipitation, erosion, and runoff, and
675 increased primary and secondary production in the coastal realm.

676 A poleward expansion of convective precipitation due to the diminished early Eocene
677 meridional temperature gradient (Speelman et al., 2010) might have led to a more proximal
678 forcing of high-latitude moisture supply. It is plausible that the humidity was sustained by deep
679 convection happening in the high latitudes, as suggested by certain model simulations of ice-free
680 polar conditions (Abbot and Tziperman, 2008a, 2008b), and presumably strongly influenced by
681 summer insolation, possibly even resulting in a monsoon-like climate at high latitudes (Baatsen
682 et al., 2024). Interestingly, such high latitude deep convection might present an important
683 feedback mechanism for extratropical amplification of climate variability, and maintaining
684 above-freezing winter temperatures (Abbot and Tziperman, 2008a). This mechanism starkly
685 contrasts the Pleistocene situation, when obliquity modulated the moisture transport from lower
686 latitudes through insolation gradients (Vimeux et al., 2001; Masson-Delmotte et al., 2005), while
687 polar temperatures predominantly varied in-phase with insolation (Kindler et al., 2014; Uemura
688 et al., 2018). Hence, it can be argued that the effects of (sea) ice cover, high albedo and much
689 colder high-latitude SSTs in the Pleistocene greatly minimized the effects of high-latitude
690 summer insolation maxima on hydrological processes, while they were dominant in the early
691 Eocene.

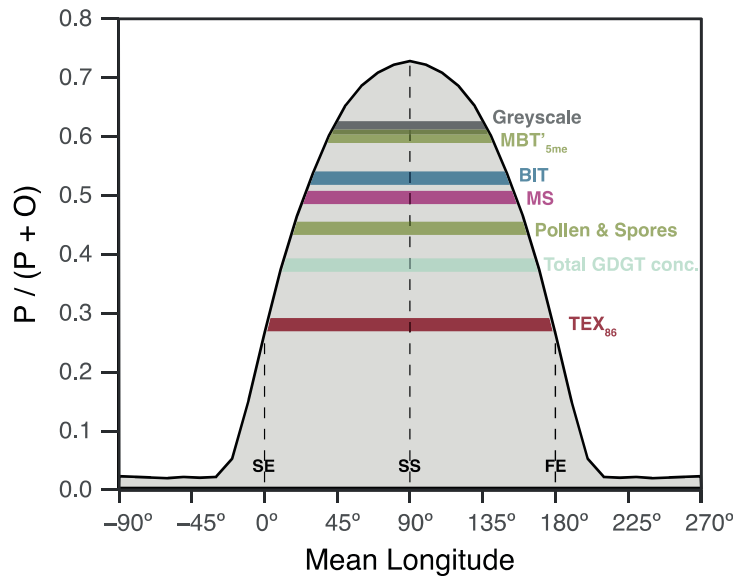
692 As noted in previous work, the PETM and ETM2 events in the early Eocene Arctic were
693 paired with massive hydrological changes (Sluijs et al., 2006, 2009; Pagani et al., 2006; Krishnan
694 et al., 2014), here corroborated by our higher resolution biomarker and palynology data.
695 Interestingly, our orbital age model now allows for determining sedimentation rate changes.
696 Based on our determined background sedimentation rates of 0.5 cm/kyr and the 56 cm interval
697 covering the peak ETM2 CIE and recovery at Lomonosov Ridge, which corresponds to a ~60
698 kyr time interval (Stap et al., 2010), we infer a factor 1.8 sedimentation rate increase to ~0.9
699 cm/kyr. While this accumulation rate increase is smaller than the recorded three- to fivefold
700 increase during the PETM (Sluijs et al., 2008b), together with the enhanced iron accumulation it
701 confirms the increased terrestrial sediment supply during the event, likely due to an intensified
702 hydrological cycle.

703 5.4 Seasonality of the proxy records

704 Variations in Earth's axial precession have multiple implications for the insolation that
705 reaches Earth. The first order control is the proximity to the sun, as precession determines the
706 season that coincides with peri/aphelion. However, due to conservation of angular momentum,
707 Earth moves faster when it is closer to the sun and the season at perihelion is therefore also the
708 shortest season (Loutre et al., 2004). Consequently, if insolation is averaged across the complete
709 summer, this effect almost entirely counters the positive effect of perihelion during summer
710 solstice (Huybers, 2006). Obliquity, on the other hand, has a more straight-forward effect on
711 regional insolation, especially in the polar regions, where its direct effect is restricted to mainly

712 influencing summer radiation. Together, due to their different mechanisms, the relative imprint
 713 of obliquity and precession on a climatic parameter depends on the duration and season of
 714 forcing (see **Fig. 2**).

715



716

717 **Figure 8.** Precession/obliquity index of insolation for different periods surrounding the summer
 718 solstice. Positions of the spring equinox, summer solstice and fall equinox are marked by dashed
 719 lines. Plot based on MTM spectra of La04 insolation curve (Laskar et al., 2004) at 78°N during
 720 the pre-ETM2 interval. SE = spring equinox, SS = summer solstice, FE = fall equinox.

721

722 When we assume a direct coupling between local insolation and proxy response, and a
 723 forcing centered around the summer solstice, the precession and obliquity index distribution at
 724 78°N (precession / (precession + obliquity; $P / (P + O)$) has a bell-shaped pattern (Fig. 8). Similar
 725 index values, calculated from spectral amplitudes from our proxy records, show that our orbital
 726 proxy variability is forced by different orbital components, some that show strong imprint of
 727 precession (e.g., greyscale and MBT'_{5me}), and some with much stronger obliquity (TEX_{86} and
 728 total GDGT concentration). Crucially, the TEX_{86} spectrum dominantly shows obliquity and very
 729 low (or absent) precession ($P / (P + O) = 0.28$), which takes it very far from a short (peak)
 730 summer forcing. Rather, a forcing from start of spring to start of fall is more in line with the
 731 orbital imprint. Note that, as the precession component of the TEX_{86} frequency spectrum is
 732 below the 0.9 CI of AR(1) noise (Fig. 4), the forcing period is essentially indistinguishable from
 733 annual averaged forcing (Fig. 8). However, the clear expression of multiple precession cycles in
 734 the filtered TEX_{86} record during certain eccentricity maxima (e.g., at 54.350 and 54.250, Fig. 7)
 735 suggest that a small component of precession is indeed present, and corroborates the spring–fall
 736 forcing of this signal.

737

738

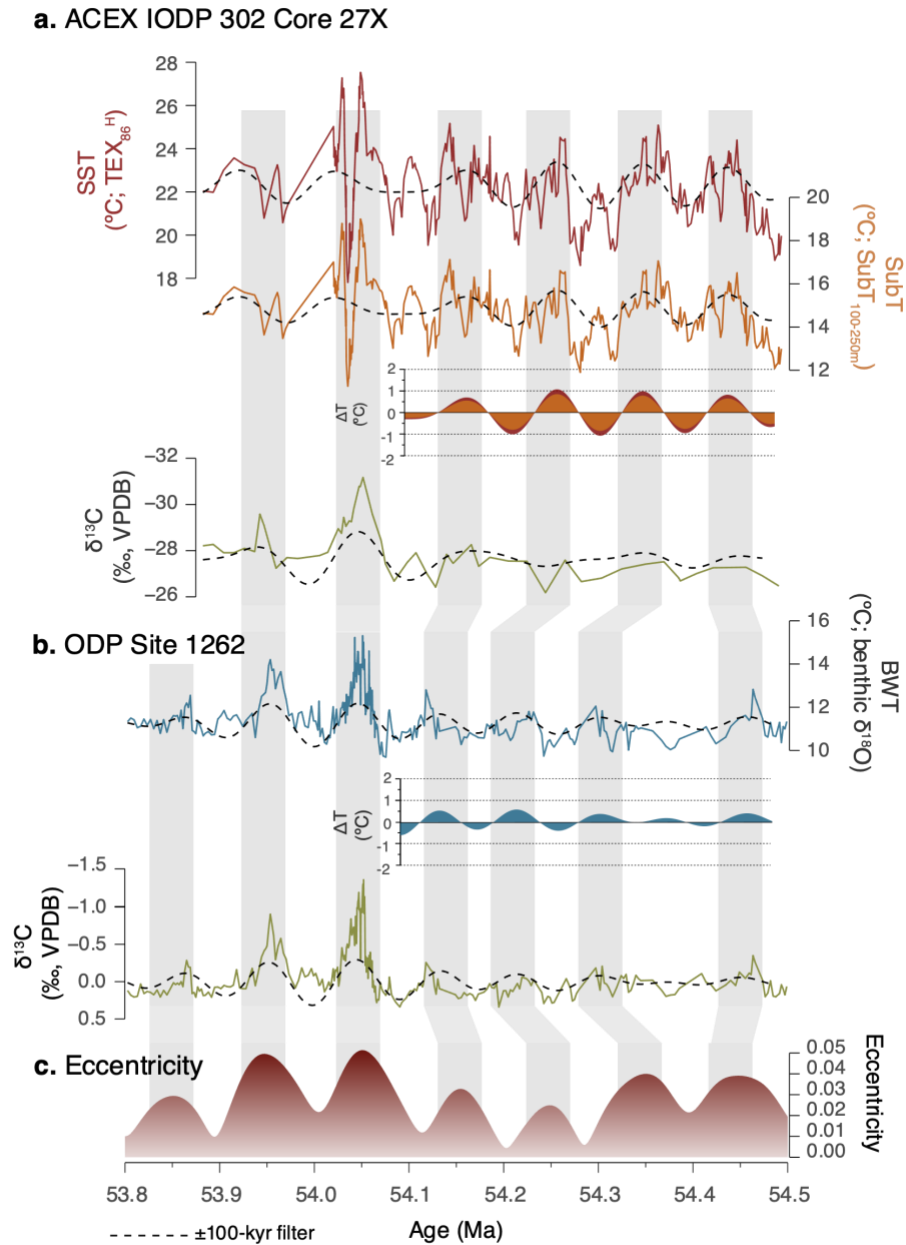
739 The other signals (i.e., greyscale, MBT'_{5me}, BIT, MS, Pollen & Spores, GDGT
740 concentration) associated with hydrological variability on land and associated marine
741 productivity have higher relative influence of precession. The signals with higher influence of
742 precession implies that either the period of forcing was a shorter period around the solstice, or
743 that it was more skewed towards one season. The dominant imprint of precession on the
744 hydrological indicators at the Lomonosov Ridge could therefore resemble a mechanism that is
745 reminiscent of precession influenced low-latitude monsoonal systems, where summer insolation
746 maxima dominate monsoon intensity (Kutzbach and Otto-Bliesner, 1982; Kutzbach et al., 2008).
747 A strong seasonal precipitation in the early Eocene Arctic, as our orbital interpretation suggests,
748 has been supported by strong seasonal $\delta^{13}\text{C}$ variations in fossilized wood (Schubert et al., 2012),
749 but is contrasted by fossil leaf and pollen analyses (West et al., 2015; Willard et al., 2019).

750 5.5 Arctic endmember of eccentricity-forced global temperature variability

751 The imprint of 100-kyr orbital eccentricity on pre-ETM2 SSTs at the Lomonosov Ridge
752 margin, while the direct influence of eccentricity on insolation is minor, confirms previous
753 studies of the early Eocene that find high imprint of this cycle on temperature variability (e.g.,
754 Laurentano et al., 2018; Fokkema et al., 2023), even if the major imprint of eccentricity on the
755 occurrence of hyperthermals is ignored. We analyze the imprint of the short-eccentricity cycle on
756 temperature during the pre-ETM2 interval by comparing the signal of ACEX to that
757 reconstructed by benthic foraminiferal carbonate oxygen isotope ratios from Walvis Ridge ODP
758 Site 1262 (Stap et al., 2010; Littler et al., 2014). While the resolution of the benthic isotope
759 records is suboptimal in the pre-ETM2 interval, we find an amplitude of eccentricity variability
760 of ~ 0.3 °C (Fig. 9; Supp. Fig. S6), which is 2 – 3 times smaller than our recorded variability
761 (~ 0.7 – 0.8 °C) at the Lomonosov Ridge. While both records reflect high latitude signals, the
762 higher latitude of the ACEX (78° N) compared to the bottom-water formation areas in the
763 Southern Ocean (~ 60 – 65 °S; Lunt et al., 2021) could lead to an amplified signal at ACEX,
764 however the magnitude of amplification remains high.

765 In lack of contemporary tropical SST records, we additionally compare to a record from
766 the tropical Atlantic that just succeeds the studied pre-ETM2 interval (53.7–52.0 Ma) from the
767 Eastern Equatorial Atlantic (Fokkema et al., 2023) (Site 959; paleolatitude = $\sim 9^\circ\text{S}$). At Ocean
768 Drilling Program (ODP) Site 959, the amplitude of SST variability associated with short-
769 eccentricity outside the hyperthermals is approximately 0.2–0.3 °C. The significantly higher
770 variability that we reported compared to the tropics suggests that the temperature variations
771 associated with short-term eccentricity were amplified by a factor of 3–4 at Lomonosov Ridge
772 margin compared to the tropical Atlantic Ocean.

773



774

775 **Figure 9.** Comparison of eccentricity-scale temperature variability between this study and the
 776 open ocean benthic record of ODP Site 1262. **(a)** ACEX SST/SubT with 100-kyr eccentricity
 777 filters, and organic δ¹³C record. **(b)** Open ocean bottom water temperatures (BWTs) and δ¹³C
 778 from ODP 1262, with 100-kyr eccentricity filters. BWTs are based on benthic foraminiferal
 779 δ¹⁸O. **(c)** Orbital eccentricity (Laskar et al., 2011). For ODP Site 1262, minor deviations of the
 780 age model by Westerhold et al., (2017) were made to line up the δ¹³C and δ¹⁸O minima with the
 781 eccentricity maxima. The amplitude of SST variability from the ACEX is presented as a range,
 782 using both an SST (TEX₈₆^H) and SubT (SubT_{100-250m}) calibration.

783

784 **6. Conclusions**

785 The high-resolution organic biomarker, palynological and geochemical analyses
786 presented in this work allow for the reconstruction of complete Milankovitch climate variability
787 at the early Eocene Lomonosov Ridge. Insolation variability invoked by obliquity and precession
788 cyclicity caused temperature variations up to 1.0–1.4 and 0.4–0.6 °C, respectively. Utilizing the
789 relative spectral amplitudes of the precession and obliquity frequencies in the TEX₈₆ record, we
790 infer that the reconstructed temperature variability represents a spring-to-fall forced signal.

791 The TEX₈₆ maxima correlate to maxima in terrestrial organic supply to the Arctic basin,
792 notably evidenced by peak abundances in terrestrial palynomorphs, suggesting that regional
793 insolation maxima (precession minima / obliquity maxima) dominated hydrological processes in
794 the Arctic region, causing enhanced precipitation, continental runoff and nutrient input into the
795 basin, and triggering highly productive conditions at the central Lomonosov Ridge. The in-phase
796 relationship on obliquity timescales suggests that regional moisture circulation was the dominant
797 forcing agent on the orbital hydrological response, in contrast to meridional moisture transport
798 which dominated precipitation on orbital timescales in the Pleistocene.

799 Temperature variations paced by Earth's orbital eccentricity maxima greatly impacted
800 Arctic temperatures as well. Next to the globally defined ETM2 event, where Lomonosov Ridge
801 experienced ~5 °C warming, 100-kyr orbital eccentricity led to an amplitude of SST variation of
802 0.7 – 0.8 °C, 2–3 times higher than synchronous temperature variations recorded in the deep
803 Atlantic Ocean. Compared to 100-kyr related variability in the tropical Atlantic (Fokkema et al.
804 2023), our amplitude suggests an amplification of this signal by a factor 3–4, much higher than
805 previous early Eocene estimates of polar amplification of climate change. Importantly, by
806 reconstructing the complete imprint of Milankovitch forcing on Arctic temperature variability,
807 potential bias towards one end of the orbital climate variability can be excluded.

808

809 **7. Acknowledgments**

810 This work used samples retrieved by the International Ocean Discovery Program. We
811 thank for Dr. H. Kuhlmann at Bremen Core Repository for providing the u-channels and core-
812 catcher samples. We thank Antoinette van den Dikkenberg, Martin Luijendijk, Harvey de Graaf,
813 Natasja Welters, Giovanni Dammers and Maxim Krasnoperov for their assistance in the lab and
814 Lucas Lourens for discussions on the spectral analysis and tuning. We also thank the members of
815 the ACEX scientific party. This work was funded by the European Research Council through
816 Consolidator Grant 771497 awarded to AS under the Horizon 2020 program. This study
817 benefitted from intellectual contributions by members of the Netherlands Earth System Science
818 Centre, funded by Gravitation Grant 024.002.001 from the Dutch Ministry of Education, Culture
819 and Science.

820

821 **Open Research**

822 All data presented in this work will be made openly available on zenodo.org.

823

824 **References**

- 825 Abbot, D. S., & Tziperman, E. (2008). Sea ice, high-latitude convection, and equable
826 climates. *Geophysical Research Letters*, 35(3), 2007GL032286.
827 <https://doi.org/10.1029/2007GL032286>
- 828 Abbot, Dorian S., & Tziperman, E. (2008). A high-latitude convective cloud feedback
829 and equable climates. *Quarterly Journal of the Royal Meteorological Society*, 134(630), 165–
830 185. <https://doi.org/10.1002/qj.211>
- 831 Anagnostou, E., John, E. H., Babila, T. L., Sexton, P. F., Ridgwell, A., Lunt, D. J., et al.
832 (2020). Proxy evidence for state-dependence of climate sensitivity in the Eocene greenhouse.
833 *Nature Communications*, 11(1), 4436. <https://doi.org/10.1038/s41467-020-17887-x>
- 834 Baatsen, M., Bijl, P., Von Der Heydt, A., Sluijs, A., & Dijkstra, H. (2024). Resilient
835 Antarctic monsoonal climate prevented ice growth during the Eocene. *Climate of the Past*, 20(1),
836 77–90. <https://doi.org/10.5194/cp-20-77-2024>
- 837 Backman, J., Moran, K., McInroy, D. B., Mayer, L. A., & Expedition 302 Scientists
838 (Eds.). (2006). *Proceedings of the IODP, 302 (Vol. 302). Integrated Ocean Drilling Program.*
839 <https://doi.org/10.2204/iodp.proc.302.2006>
- 840 Barke, J., Abels, H. A., Sangiorgi, F., Greenwood, D. R., Sweet, A. R., Donders, T., et al.
841 (2011). Orbitally forced Azolla blooms and Middle Eocene Arctic hydrology: Clues from
842 palynology. *Geology*, 39(5), 427–430. <https://doi.org/10.1130/G31640.1>
- 843 Bijl, P. K., Schouten, S., Sluijs, A., Reichart, G.-J., Zachos, J. C., & Brinkhuis, H. (2009).
844 Early Palaeogene temperature evolution of the southwest Pacific Ocean. *Nature*, 461(7265),
845 776–779. <https://doi.org/10.1038/nature08399>
- 846 Bijl, P. K., Frieling, J., Cramwinckel, M. J., Boschman, C., Sluijs, A., & Peterse, F.
847 (2021). Maastrichtian–Rupelian paleoclimates in the southwest Pacific – a critical re-evaluation
848 of biomarker paleothermometry and dinoflagellate cyst paleoecology at Ocean Drilling Program
849 Site 1172. *Climate of the Past*, 17(6), 2393–2425. <https://doi.org/10.5194/cp-17-2393-2021>
- 850 Blaga, C. I., Reichart, G.-J., Heiri, O., & Sinninghe Damsté, J. S. (2009). Tetraether
851 membrane lipid distributions in water-column particulate matter and sediments: a study of 47
852 European lakes along a north–south transect. *Journal of Paleolimnology*, 41(3), 523–540.
853 <https://doi.org/10.1007/s10933-008-9242-2>
- 854 Browning, J. V., Miller, K. G., & Pak, D. K. (1996). Global implications of lower to
855 middle Eocene sequence boundaries on the New Jersey coastal plain: The icehouse cometh.
856 *Geology*, 24(7), 639. [https://doi.org/10.1130/0091-7613\(1996\)024<0639:GIOLTM>2.3.CO;2](https://doi.org/10.1130/0091-7613(1996)024<0639:GIOLTM>2.3.CO;2)
- 857 Carton, J. A., Ding, Y., & Arrigo, K. R. (2015). The seasonal cycle of the Arctic Ocean
858 under climate change. *Geophysical Research Letters*, 42(18), 7681–7686.
859 <https://doi.org/10.1002/2015GL064514>
- 860 Cramer, B. S., Wright, J. D., Kent, D. V., & Aubry, M.-P. (2003). Orbital climate forcing
861 of $\delta^{13}\text{C}$ excursions in the late Paleocene—early Eocene (chrons C24n–C25n).
862 *Paleoceanography*, 18, 1097. <https://doi.org/10.1029/2003PA000909>

- 863 Cramwinckel, M. J., Huber, M., Kocken, I. J., Agnini, C., Bijl, P. K., Bohaty, S. M., et al.
864 (2018). Synchronous tropical and polar temperature evolution in the Eocene. *Nature*, 559(7714),
865 382–386. <https://doi.org/10.1038/s41586-018-0272-2>
- 866 Cramwinckel, M. J., Burls, N. J., Fahad, A. A., Knapp, S., West, C. K., Reichgelt, T., et
867 al. (2023). Global and Zonal-Mean Hydrological Response to Early Eocene Warmth.
868 *Paleoceanography and Paleoclimatology*, 38(6), e2022PA004542.
869 <https://doi.org/10.1029/2022PA004542>
- 870 De Jonge, C., Hopmans, E. C., Zell, C. I., Kim, J.-H., Schouten, S., & Sinninghe Damsté,
871 J. S. (2014). Occurrence and abundance of 6-methyl branched glycerol dialkyl glycerol
872 tetraethers in soils: Implications for palaeoclimate reconstruction. *Geochimica et Cosmochimica*
873 *Acta*, 141, 97–112. <https://doi.org/10.1016/j.gca.2014.06.013>
- 874 Dearing Crampton-Flood, E., Tierney, J. E., Peterse, F., Kirkels, F. M. S. A., &
875 Sinninghe Damsté, J. S. (2020). BayMBT: A Bayesian calibration model for branched glycerol
876 dialkyl glycerol tetraethers in soils and peats. *Geochimica et Cosmochimica Acta*, 268, 142–159.
877 <https://doi.org/10.1016/j.gca.2019.09.043>
- 878 Dickens, G. R., O’Neil, J. R., Rea, D. K., & Owen, R. M. (1995). Dissociation of oceanic
879 methane hydrate as a cause of the carbon isotope excursion at the end of the Paleocene.
880 *Paleoceanography*, 10(6), 965–971. <https://doi.org/10.1029/95PA02087>
- 881 Dickens, G. R., Castillo, M. M., & Walker, J. C. G. (1997). A blast of gas in the latest
882 Paleocene: Simulating first-order effects of massive dissociation of oceanic methane hydrate.
883 *Geology*, 25(3), 259. [https://doi.org/10.1130/0091-7613\(1997\)025<0259:ABOGIT>2.3.CO;2](https://doi.org/10.1130/0091-7613(1997)025<0259:ABOGIT>2.3.CO;2)
- 884 Evans, D., Sagoo, N., Renema, W., Cotton, L. J., Müller, W., Todd, J. A., et al. (2018).
885 Eocene greenhouse climate revealed by coupled clumped isotope-Mg/Ca thermometry.
886 *Proceedings of the National Academy of Sciences*, 115(6), 1174–1179.
887 <https://doi.org/10.1073/pnas.1714744115>
- 888 Fokkema, C. D., Agterhuis, T., Gerritsma, D., De Goeij, M., Liu, X., De Regt, P., et al.
889 (2023). Polar amplification of orbital-scale climate variability in the early Eocene greenhouse
890 world (Preprint). *Climate of the Past Discussions*. <https://doi.org/10.5194/cp-2023-70>
- 891 Frieling, J., & Sluijs, A. (2018). Towards quantitative environmental reconstructions
892 from ancient non-analogue microfossil assemblages: Ecological preferences of Paleocene –
893 Eocene dinoflagellates. *Earth-Science Reviews*, 185, 956–973.
894 <https://doi.org/10.1016/j.earscirev.2018.08.014>
- 895 Galeotti, S., Krishnan, S., Pagani, M., Lanci, L., Gaudio, A., Zachos, J. C., et al. (2010).
896 Orbital chronology of Early Eocene hyperthermals from the Contessa Road section, central Italy.
897 *Earth and Planetary Science Letters*, 290(1–2), 192–200.
898 <https://doi.org/10.1016/j.epsl.2009.12.021>
- 899 Ho, S. L., & Laepple, T. (2016). Flat meridional temperature gradient in the early Eocene
900 in the subsurface rather than surface ocean. *Nature Geoscience*, 9(8), 606–610.
901 <https://doi.org/10.1038/ngeo2763>
- 902 Hopmans, E. C., Weijers, J. W. H., Schefuß, E., Herfort, L., Sinninghe Damsté, J. S., &
903 Schouten, S. (2004). A novel proxy for terrestrial organic matter in sediments based on branched

- 904 and isoprenoid tetraether lipids. *Earth and Planetary Science Letters*, 224(1–2), 107–116.
905 <https://doi.org/10.1016/j.epsl.2004.05.012>
- 906 Hopmans, E. C., Schouten, S., & Sinninghe Damsté, J. S. (2016). The effect of improved
907 chromatography on GDGT-based palaeoproxies. *Organic Geochemistry*, 93, 1–6.
908 <https://doi.org/10.1016/j.orggeochem.2015.12.006>
- 909 Hurley, S. J., Lipp, J. S., Close, H. G., Hinrichs, K.-U., & Pearson, A. (2018).
910 Distribution and export of isoprenoid tetraether lipids in suspended particulate matter from the
911 water column of the Western Atlantic Ocean. *Organic Geochemistry*, 116, 90–102.
912 <https://doi.org/10.1016/j.orggeochem.2017.11.010>
- 913 Huybers, P. (2006). Early Pleistocene Glacial Cycles and the Integrated Summer
914 Insolation Forcing. *Science*, 313(5786), 508–511. <https://doi.org/10.1126/science.1125249>
- 915 Inglis, G. N., Bragg, F., Burls, N. J., Cramwinckel, M. J., Evans, D., Foster, G. L., et al.
916 (2020). Global mean surface temperature and climate sensitivity of the early Eocene Climatic
917 Optimum (EECO), Paleocene–Eocene Thermal Maximum (PETM), and latest Paleocene.
918 *Climate of the Past*, 16(5), 1953–1968. <https://doi.org/10.5194/cp-16-1953-2020>
- 919 Kennett, J. P., & Stott, L. D. (1991). Abrupt deep-sea warming, palaeoceanographic
920 changes and benthic extinctions at the end of the Palaeocene. *Nature*, 353(6341), 225–229.
921 <https://doi.org/10.1038/353225a0>
- 922 Kim, J.-H., van der Meer, J., Schouten, S., Helmke, P., Willmott, V., Sangiorgi, F., et al.
923 (2010). New indices and calibrations derived from the distribution of crenarchaeal isoprenoid
924 tetraether lipids: Implications for past sea surface temperature reconstructions. *Geochimica et*
925 *Cosmochimica Acta*, 74(16), 4639–4654. <https://doi.org/10.1016/j.gca.2010.05.027>
- 926 Kindler, P., Guillevic, M., Baumgartner, M., Schwander, J., Landais, A., & Leuenberger,
927 M. (2014). Temperature reconstruction from 10 to 120 kyr b2k from the NGRIP ice core.
928 *Climate of the Past*, 10(2), 887–902. <https://doi.org/10.5194/cp-10-887-2014>
- 929 Kocken, I. J. (2022). colourlog: generate plots of colourlogs from core photographs.
930 <https://doi.org/10.5281/zenodo.7277860>
- 931 Krishnan, S., Pagani, M., Huber, M., & Sluijs, A. (2014). High latitude hydrological
932 changes during the Eocene Thermal Maximum 2. *Earth and Planetary Science Letters*, 404, 167–
933 177. <https://doi.org/10.1016/j.epsl.2014.07.029>
- 934 Kutzbach, J. E., & Otto-Bliesner, B. L. (1982). The sensitivity of the African-Asian
935 monsoonal climate to orbital parameter changes for 9000 years BP in a low-resolution general
936 circulation model. *Journal of Atmospheric Sciences*, 39(6), 1177–1188.
- 937 Kutzbach, J. E., Liu, X., Liu, Z., & Chen, G. (2008). Simulation of the evolutionary
938 response of global summer monsoons to orbital forcing over the past 280,000 years. *Climate*
939 *Dynamics*, 30(6), 567–579. <https://doi.org/10.1007/s00382-007-0308-z>
- 940 Laskar, J., Robutel, P., Joutel, F., Gastineau, M., Correia, A. C. M., & Levrard, B. (2004).
941 A long-term numerical solution for the insolation quantities of the Earth. *Astronomy &*
942 *Astrophysics*, 428(1), 261–285. <https://doi.org/10.1051/0004-6361:20041335>

- 943 Laskar, J., Fienga, A., Gastineau, M., & Manche, H. (2011). La2010: a new orbital
944 solution for the long-term motion of the Earth. *Astronomy & Astrophysics*, 532, A89.
945 <https://doi.org/10.1051/0004-6361/201116836>
- 946 Lauretano, V., Zachos, J. C., & Lourens, L. J. (2018). Orbitally Paced Carbon and Deep-
947 Sea Temperature Changes at the Peak of the Early Eocene Climatic Optimum. *Paleoceanography*
948 *and Paleoclimatology*, 33(10), 1050–1065. <https://doi.org/10.1029/2018PA003422>
- 949 Li, M., Hinnov, L., & Kump, L. (2019). Acycle: Time-series analysis software for
950 paleoclimate research and education. *Computers & Geosciences*, 127, 12–22.
951 <https://doi.org/10.1016/j.cageo.2019.02.011>
- 952 Littler, K., Röhl, U., Westerhold, T., & Zachos, J. C. (2014). A high-resolution benthic
953 stable-isotope record for the South Atlantic: Implications for orbital-scale changes in Late
954 Paleocene–Early Eocene climate and carbon cycling. *Earth and Planetary Science Letters*, 401,
955 18–30. <https://doi.org/10.1016/j.epsl.2014.05.054>
- 956 Lourens, L. J., Sluijs, A., Kroon, D., Zachos, J. C., Thomas, E., Röhl, U., et al. (2005).
957 Astronomical pacing of late Palaeocene to early Eocene global warming events. *Nature*,
958 435(7045), 1083–1087. <https://doi.org/10.1038/nature03814>
- 959 Lourens, L. J., Becker, J., Bintanja, R., Hilgen, F. J., Tüenter, E., Van De Wal, R. S. W.,
960 & Ziegler, M. (2010). Linear and non-linear response of late Neogene glacial cycles to obliquity
961 forcing and implications for the Milankovitch theory. *Quaternary Science Reviews*, 29(1–2),
962 352–365. <https://doi.org/10.1016/j.quascirev.2009.10.018>
- 963 Loutre, M.-F., Paillard, D., Vimeux, F., & Cortijo, E. (2004). Does mean annual
964 insolation have the potential to change the climate? *Earth and Planetary Science Letters*, 221(1–
965 4), 1–14. [https://doi.org/10.1016/S0012-821X\(04\)00108-6](https://doi.org/10.1016/S0012-821X(04)00108-6)
- 966 Lunt, D. J., Bragg, F., Chan, W.-L., Hutchinson, D. K., Ladant, J.-B., Morozova, P., et al.
967 (2021). DeepMIP: Model intercomparison of early Eocene climatic optimum (EECO) large-scale
968 climate features and comparison with proxy data. *Climate of the Past*, 17, 203–227.
- 969 Martínez-Sosa, P., Tierney, J. E., Pérez-Angel, L. C., Stefanescu, I. C., Guo, J., Kirkels,
970 F., et al. (2023). Development and Application of the Branched and Isoprenoid GDGT Machine
971 Learning Classification Algorithm (BIGMaC) for Paleoenvironmental Reconstruction.
972 *Paleoceanography and Paleoclimatology*, 38(7), e2023PA004611.
973 <https://doi.org/10.1029/2023PA004611>
- 974 Massana, R., DeLong, E. F., & Pedrós-Alió, C. (2000). A Few Cosmopolitan Phylotypes
975 Dominate Planktonic Archaeal Assemblages in Widely Different Oceanic Provinces. *Applied*
976 *and Environmental Microbiology*, 66(5), 1777–1787. [https://doi.org/10.1128/AEM.66.5.1777-](https://doi.org/10.1128/AEM.66.5.1777-1787.2000)
977 [1787.2000](https://doi.org/10.1128/AEM.66.5.1777-1787.2000)
- 978 Masson-Delmotte, V., Jouzel, J., Landais, A., Stievenard, M., Johnsen, S. J., White, J. W.
979 C., et al. (2005). GRIP Deuterium Excess Reveals Rapid and Orbital-Scale Changes in
980 Greenland Moisture Origin. *Science*, 309(5731), 118–121.
981 <https://doi.org/10.1126/science.1108575>
- 982 Pagani, M., Pedentchouk, N., Huber, M., Sluijs, A., Schouten, S., Brinkhuis, H., et al.
983 (2006). Arctic hydrology during global warming at the Palaeocene/Eocene thermal maximum.
984 *Nature*, 442(7103), 671–675. <https://doi.org/10.1038/nature05043>

- 985 Pälike, H., Spofforth, D. J. A., O'Regan, M., & Gattacceca, J. (2008). Orbital scale
986 variations and timescales from the Arctic Ocean. *Paleoceanography*, 23(1), PA1S10.
987 <https://doi.org/10.1029/2007PA001490>
- 988 Peterse, F., Kim, J.-H., Schouten, S., Kristensen, D. K., Koç, N., & Sinninghe Damsté, J.
989 S. (2009). Constraints on the application of the MBT/CBT palaeothermometer at high latitude
990 environments (Svalbard, Norway). *Organic Geochemistry*, 40(6), 692–699.
991 <https://doi.org/10.1016/j.orggeochem.2009.03.004>
- 992 Powell, A. J., Brinkhuis, H., & Bujak, J. P. (1996). Upper Paleocene-Lower Eocene
993 dinoflagellate cyst sequence biostratigraphy of southeast England. Geological Society, London,
994 Special Publications, 101(1), 145–183. <https://doi.org/10.1144/GSL.SP.1996.101.01.10>
- 995 Rattanasriampaipong, R., Zhang, Y. G., Pearson, A., Hedlund, B. P., & Zhang, S. (2022).
996 Archaeal lipids trace ecology and evolution of marine ammonia-oxidizing archaea. *Proceedings*
997 *of the National Academy of Sciences*, 119(31), e2123193119.
998 <https://doi.org/10.1073/pnas.2123193119>
- 999 Raymo, M. E., & Nisancioglu, K. H. (2003). The 41 kyr world: Milankovitch's other
1000 unsolved mystery. *Paleoceanography*, 18(1), 2002PA000791.
1001 <https://doi.org/10.1029/2002PA000791>
- 1002 Sangiorgi, F., van Soelen, E. E., Spofforth, D. J. A., Pälike, H., Stickley, C. E., St. John,
1003 K., et al. (2008). Cyclicity in the middle Eocene central Arctic Ocean sediment record: Orbital
1004 forcing and environmental response. *Paleoceanography*, 23(1).
1005 <https://doi.org/10.1029/2007PA001487>
- 1006 Schouten, S., Hopmans, E. C., Schefuß, E., & Sinninghe Damsté, J. S. (2002).
1007 Distributional variations in marine crenarchaeotal membrane lipids: a new tool for reconstructing
1008 ancient sea water temperatures? *Earth and Planetary Science Letters*, 204(1–2), 265–274.
1009 [https://doi.org/10.1016/S0012-821X\(02\)00979-2](https://doi.org/10.1016/S0012-821X(02)00979-2)
- 1010 Schubert, B. A., Jahren, A. H., Eberle, J. J., Sternberg, L. S. L., & Eberth, D. A. (2012).
1011 A summertime rainy season in the Arctic forests of the Eocene. *Geology*, 40(6), 523–526.
1012 <https://doi.org/10.1130/G32856.1>
- 1013 Sinninghe Damsté, J. S. (2016). Spatial heterogeneity of sources of branched tetraethers
1014 in shelf systems: The geochemistry of tetraethers in the Berau River delta (Kalimantan,
1015 Indonesia). *Geochimica et Cosmochimica Acta*, 186, 13–31.
1016 <https://doi.org/10.1016/j.gca.2016.04.033>
- 1017 Sinninghe Damsté, J. S., Rijpstra, W. I. C., Hopmans, E. C., Prahl, F. G., Wakeham, S.
1018 G., & Schouten, S. (2002). Distribution of Membrane Lipids of Planktonic Crenarchaeota in the
1019 Arabian Sea. *Applied and Environmental Microbiology*, 68(6), 2997–3002.
1020 <https://doi.org/10.1128/AEM.68.6.2997-3002.2002>
- 1021 Sluijs, A., & Brinkhuis, H. (2009). A dynamic climate and ecosystem state during the
1022 Paleocene-Eocene Thermal Maximum: inferences from dinoflagellate cyst assemblages on the
1023 New Jersey Shelf. *Biogeosciences*, 6(8), 1755–1781. <https://doi.org/10.5194/bg-6-1755-2009>
- 1024 Sluijs, Appy, Schouten, S., Pagani, M., Woltering, M., Brinkhuis, H., Damsté, J. S. S., et
1025 al. (2006). Subtropical Arctic Ocean temperatures during the Palaeocene/Eocene thermal
1026 maximum. *Nature*, 441(7093), 610–613. <https://doi.org/10.1038/nature04668>

- 1027 Sluijs, Appy, Röhl, U., Schouten, S., Brumsack, H.-J., Sangiorgi, F., Sinninghe Damsté,
1028 J. S., & Brinkhuis, H. (2008). Arctic late Paleocene-early Eocene paleoenvironments with special
1029 emphasis on the Paleocene-Eocene thermal maximum (Lomonosov Ridge, Integrated Ocean
1030 Drilling Program Expedition 302). *Paleoceanography*, 23(1), PA1S11.
1031 <https://doi.org/10.1029/2007PA001495>
- 1032 Sluijs, Appy, Brinkhuis, H., Crouch, E. M., John, C. M., Handley, L., Munsterman, D., et
1033 al. (2008). Eustatic variations during the Paleocene-Eocene greenhouse world.
1034 *Paleoceanography*, 23(4), PA4216. <https://doi.org/10.1029/2008PA001615>
- 1035 Sluijs, Appy, Schouten, S., Donders, T. H., Schoon, P. L., Röhl, U., Reichart, G.-J., et al.
1036 (2009). Warm and wet conditions in the Arctic region during Eocene Thermal Maximum 2.
1037 *Nature Geoscience*, 2(11), 777–780. <https://doi.org/10.1038/ngeo668>
- 1038 Sluijs, Appy, Frieling, J., Inglis, G. N., Nierop, K. G. J., Peterse, F., Sangiorgi, F., &
1039 Schouten, S. (2020). Late Paleocene–early Eocene Arctic Ocean sea surface temperatures:
1040 reassessing biomarker paleothermometry at Lomonosov Ridge. *Climate of the Past*, 16(6), 2381–
1041 2400. <https://doi.org/10.5194/cp-16-2381-2020>
- 1042 Speelman, E. N., Sewall, J. O., Noone, D., Huber, M., Der Heydt, A. V., Damsté, J. S., &
1043 Reichart, G.-J. (2010). Modeling the influence of a reduced equator-to-pole sea surface
1044 temperature gradient on the distribution of water isotopes in the Early/Middle Eocene. *Earth and
1045 Planetary Science Letters*, 298(1–2), 57–65. <https://doi.org/10.1016/j.epsl.2010.07.026>
- 1046 Stap, L., Lourens, L. J., Thomas, E., Sluijs, A., Bohaty, S., & Zachos, J. C. (2010). High-
1047 resolution deep-sea carbon and oxygen isotope records of Eocene Thermal Maximum 2 and H2.
1048 *Geology*, 38(7), 607–610. <https://doi.org/10.1130/G30777.1>
- 1049 Stein, R., Boucsein, B., & Meyer, H. (2006). Anoxia and high primary production in the
1050 Paleogene central Arctic Ocean: First detailed records from Lomonosov Ridge. *Geophysical
1051 Research Letters*, 33(18). <https://doi.org/10.1029/2006GL026776>
- 1052 Suan, G., Popescu, S.-M., Suc, J.-P., Schnyder, J., Fauquette, S., Baudin, F., et al. (2017).
1053 Subtropical climate conditions and mangrove growth in Arctic Siberia during the early Eocene.
1054 *Geology*, 45(6), 539–542. <https://doi.org/10.1130/G38547.1>
- 1055 Taylor, K. W. R., Huber, M., Hollis, C. J., Hernandez-Sanchez, M. T., & Pancost, R. D.
1056 (2013). Re-evaluating modern and Palaeogene GDGT distributions: Implications for SST
1057 reconstructions. *Global and Planetary Change*, 108, 158–174.
1058 <https://doi.org/10.1016/j.gloplacha.2013.06.011>
- 1059 Uemura, R., Motoyama, H., Masson-Delmotte, V., Jouzel, J., Kawamura, K., Goto-
1060 Azuma, K., et al. (2018). Asynchrony between Antarctic temperature and CO₂ associated with
1061 obliquity over the past 720,000 years. *Nature Communications*, 9(1), 961.
1062 <https://doi.org/10.1038/s41467-018-03328-3>
- 1063 Varma, D., Hättig, K., Van Der Meer, M. T. J., Reichart, G., & Schouten, S. (2023).
1064 Constraining Water Depth Influence on Organic Paleotemperature Proxies Using Sedimentary
1065 Archives. *Paleoceanography and Paleoclimatology*, 38(6), e2022PA004533.
1066 <https://doi.org/10.1029/2022PA004533>
- 1067 Vimeux, F., Masson, V., Delaygue, G., Jouzel, J., Petit, J. R., & Stievenard, M. (2001). A
1068 420,000 year deuterium excess record from East Antarctica: Information on past changes in the

- 1069 origin of precipitation at Vostok. *Journal of Geophysical Research: Atmospheres*, 106(D23),
1070 31863–31873. <https://doi.org/10.1029/2001JD900076>
- 1071 Weijers, J. W. H., Schouten, S., Spaargaren, O. C., & Sinninghe Damsté, J. S. (2006).
1072 Occurrence and distribution of tetraether membrane lipids in soils: Implications for the use of the
1073 TEX86 proxy and the BIT index. *Organic Geochemistry*, 37(12), 1680–1693.
1074 <https://doi.org/10.1016/j.orggeochem.2006.07.018>
- 1075 Weijers, J. W. H., Schouten, S., Van Den Donker, J. C., Hopmans, E. C., & Sinninghe
1076 Damsté, J. S. (2007). Environmental controls on bacterial tetraether membrane lipid distribution
1077 in soils. *Geochimica et Cosmochimica Acta*, 71(3), 703–713.
1078 <https://doi.org/10.1016/j.gca.2006.10.003>
- 1079 Weijers, J. W. H., Lim, K. L. H., Aquilina, A., Sinninghe Damsté, J. S., & Pancost, R. D.
1080 (2011). Biogeochemical controls on glycerol dialkyl glycerol tetraether lipid distributions in
1081 sediments characterized by diffusive methane flux. *Geochemistry, Geophysics, Geosystems*,
1082 12(10), Q10010. <https://doi.org/10.1029/2011GC003724>
- 1083 van der Weijst, C. M. H., van der Laan, K. J., Peterse, F., Reichart, G.-J., Sangiorgi, F.,
1084 Schouten, S., et al. (2022). A 15-million-year surface- and subsurface-integrated TEX86
1085 temperature record from the eastern equatorial Atlantic. *Climate of the Past*, 18(8), 1947–1962.
1086 <https://doi.org/10.5194/cp-18-1947-2022>
- 1087 West, C. K., Greenwood, D. R., & Basinger, J. F. (2015). Was the Arctic Eocene
1088 ‘rainforest’ monsoonal? Estimates of seasonal precipitation from early Eocene megaflores from
1089 Ellesmere Island, Nunavut. *Earth and Planetary Science Letters*, 427, 18–30.
1090 <https://doi.org/10.1016/j.epsl.2015.06.036>
- 1091 Westerhold, T., Röhl, U., Pälike, H., Wilkens, R., Wilson, P. A., & Acton, G. (2014).
1092 Orbitally tuned timescale and astronomical forcing in the middle Eocene to early Oligocene.
1093 *Climate of the Past*, 10(3), 955–973. <https://doi.org/10.5194/cp-10-955-2014>
- 1094 Westerhold, T., Röhl, U., Donner, B., & Zachos, J. C. (2018). Global Extent of Early
1095 Eocene Hyperthermal Events: A New Pacific Benthic Foraminiferal Isotope Record From
1096 Shatsky Rise (ODP Site 1209). *Paleoceanography and Paleoclimatology*, 33(6), 626–642.
1097 <https://doi.org/10.1029/2017PA003306>
- 1098 Westerhold, Thomas, Röhl, U., Frederichs, T., Agnini, C., Raffi, I., Zachos, J. C., &
1099 Wilkens, R. H. (2017). Astronomical calibration of the Ypresian timescale: implications for
1100 seafloor spreading rates and the chaotic behavior of the solar system? *Climate of the Past*, 13(9),
1101 1129–1152. <https://doi.org/10.5194/cp-13-1129-2017>
- 1102 Westerhold, Thomas, Marwan, N., Drury, A. J., Liebrand, D., Agnini, C., Anagnostou,
1103 E., et al. (2020). An astronomically dated record of Earth’s climate and its predictability over the
1104 last 66 million years. *Science*, 369(6509), 1383–1387. <https://doi.org/10.1126/science.aba6853>
- 1105 Willard, D. A., Donders, T. H., Reichgelt, T., Greenwood, D. R., Sangiorgi, F., Peterse,
1106 F., et al. (2019). Arctic vegetation, temperature, and hydrology during Early Eocene transient
1107 global warming events. *Global and Planetary Change*, 178, 139–152.
1108 <https://doi.org/10.1016/j.gloplacha.2019.04.012>
- 1109 Xiao, W., Wang, Y., Zhou, S., Hu, L., Yang, H., & Xu, Y. (2016). Ubiquitous production
1110 of branched glycerol dialkyl glycerol tetraethers(brGDGTs) in global marine environments: a

- 1111 new source indicator for brGDGTs. *Biogeosciences*, 13(20), 5883–5894.
1112 <https://doi.org/10.5194/bg-13-5883-2016>
- 1113 Xiao, W., Wang, Y., Liu, Y., Zhang, X., Shi, L., & Xu, Y. (2020). Predominance of
1114 hexamethylated 6-methyl branched glycerol dialkyl glycerol tetraethers in the Mariana Trench:
1115 source and environmental implication. *Biogeosciences*, 17(7), 2135–2148.
1116 <https://doi.org/10.5194/bg-17-2135-2020>
- 1117 Zachos, J. C., Wara, M. W., Bohaty, S., Delaney, M. L., Petrizzo, M. R., Brill, A., et al.
1118 (2003). A Transient Rise in Tropical Sea Surface Temperature During the Paleocene-Eocene
1119 Thermal Maximum. *Science*, 302(5650), 1551–1554. <https://doi.org/10.1126/science.1090110>
- 1120 Zeebe, R. E., & Lourens, L. J. (2019). Solar System chaos and the Paleocene–Eocene
1121 boundary age constrained by geology and astronomy. *Science*, 365(6456), 926–929.
1122 <https://doi.org/10.1126/science.aax0612>
- 1123 Zeeden, C., Hilgen, F., Röhl, U., Seelos, K., & Lourens, L. (2015). Sediment color as a
1124 tool in cyclostratigraphy – a new application for improved data acquisition and correction from
1125 drill cores. *Newsletters on Stratigraphy*, 48(3), 277–285. <https://doi.org/10.1127/nos/2015/0064>
- 1126 Zell, C., Kim, J.-H., Moreira-Turcq, P., Abril, G., Hopmans, E. C., Bonnet, M.-P., et al.
1127 (2013). Disentangling the origins of branched tetraether lipids and crenarchaeol in the lower
1128 Amazon River: Implications for GDGT-based proxies. *Limnology and Oceanography*, 58(1),
1129 343–353. <https://doi.org/10.4319/lo.2013.58.1.0343>
- 1130 Zhang, Y. G., Zhang, C. L., Liu, X.-L., Li, L., Hinrichs, K.-U., & Noakes, J. E. (2011).
1131 Methane Index: A tetraether archaeal lipid biomarker indicator for detecting the instability of
1132 marine gas hydrates. *Earth and Planetary Science Letters*, 307(3–4), 525–534.
1133 <https://doi.org/10.1016/j.epsl.2011.05.031>
- 1134 Zhang, Y. G., Pagani, M., & Wang, Z. (2016). Ring Index: A new strategy to evaluate the
1135 integrity of TEX 86 paleothermometry. *Paleoceanography*, 31(2), 220–232.
1136 <https://doi.org/10.1002/2015PA002848>
1137



Paleoceanography and Paleoclimatology

Supporting Information for

Orbital (hydro)climate variability in the ice-free early Eocene Arctic

Chris. D. Fokkema¹, Henk Brinkhuis^{1,2}, Francien Peterse¹ & Appy Sluijs¹

1: Department of Earth Sciences, Faculty of Geoscience, Utrecht University, 3584CB Utrecht, The Netherlands

2: Royal Netherlands Institute for Sea Research (NIOZ), 1790 AB Den Burg, The Netherlands.

Contents of this file

Figures S1 to S6

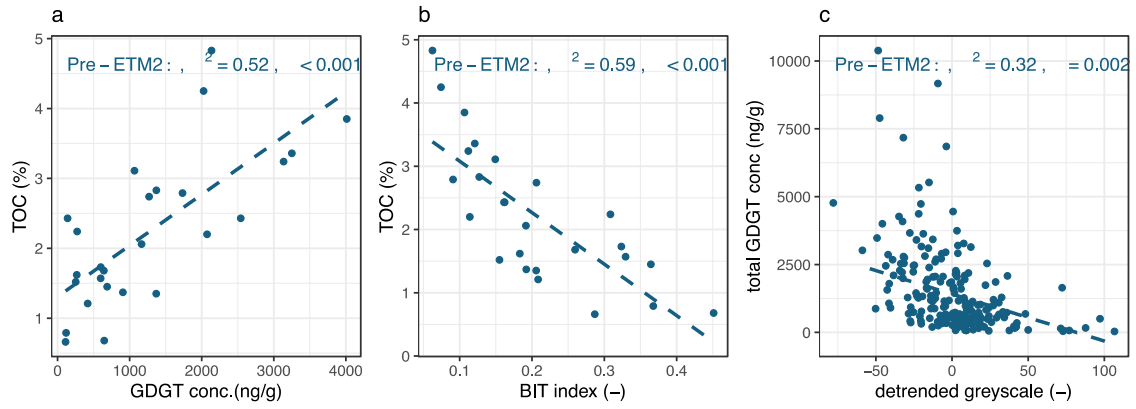


Figure S1. Cross plots between TOC% (Sluijs et al. 2009), total GDGT concentrations, BIT index, and (detrended) greyscale in the pre-ETM2 interval.

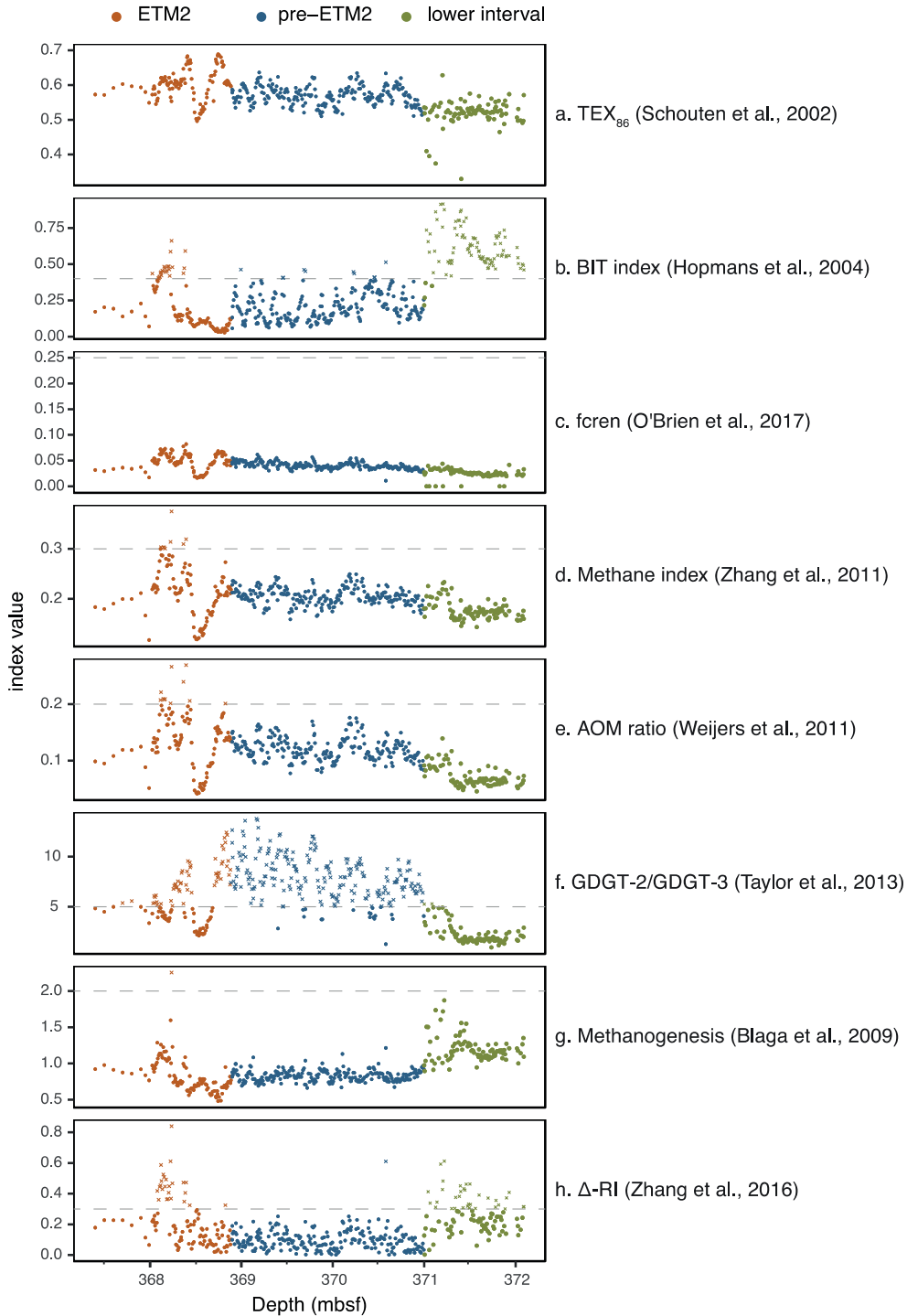


Figure S2. GDGT indices for detecting non-thermal overprint on the TEX_{86} . Dashed line indicates cut-off value for non-thermal influence maintained in literature. Colors correspond with the different intervals of Core 27X (defined in the main text). Figure generated with the R script from (Bijl et al., 2021).

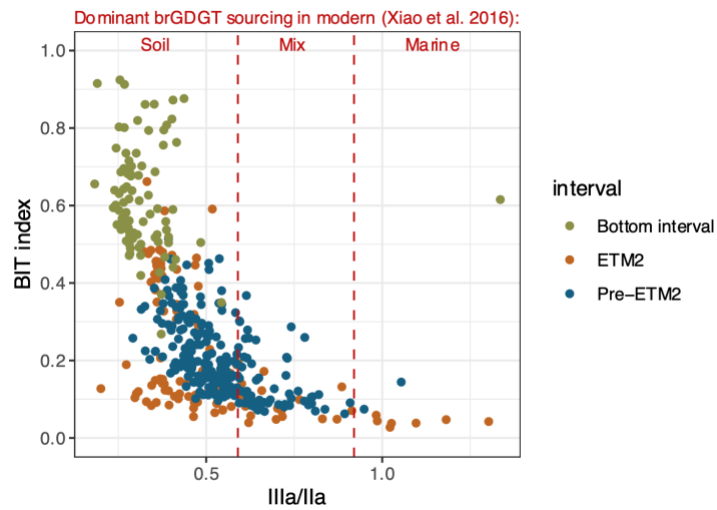


Figure S3. *IIIa/IIa* versus BIT index. Colors mark intervals, as distinguished in Main Text Section 3.1. Dominant brGDGT sources associated with *IIIa/IIa* values, as observed in the modern system by Xiao et al. (2016), are marked in red.

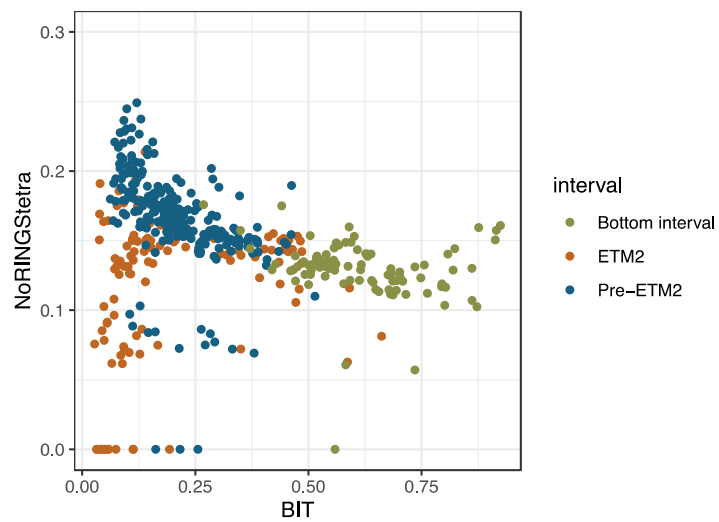


Figure S4. $\#rings_{tetra}$ versus BIT index. Colors mark intervals, as distinguished in Main Text Section 3.1. Values with $\#rings_{tetra} = 0$ ($n = 16$) relate to samples where none of the cyclic brGDGT peaks exceeded the maintained detection limit.

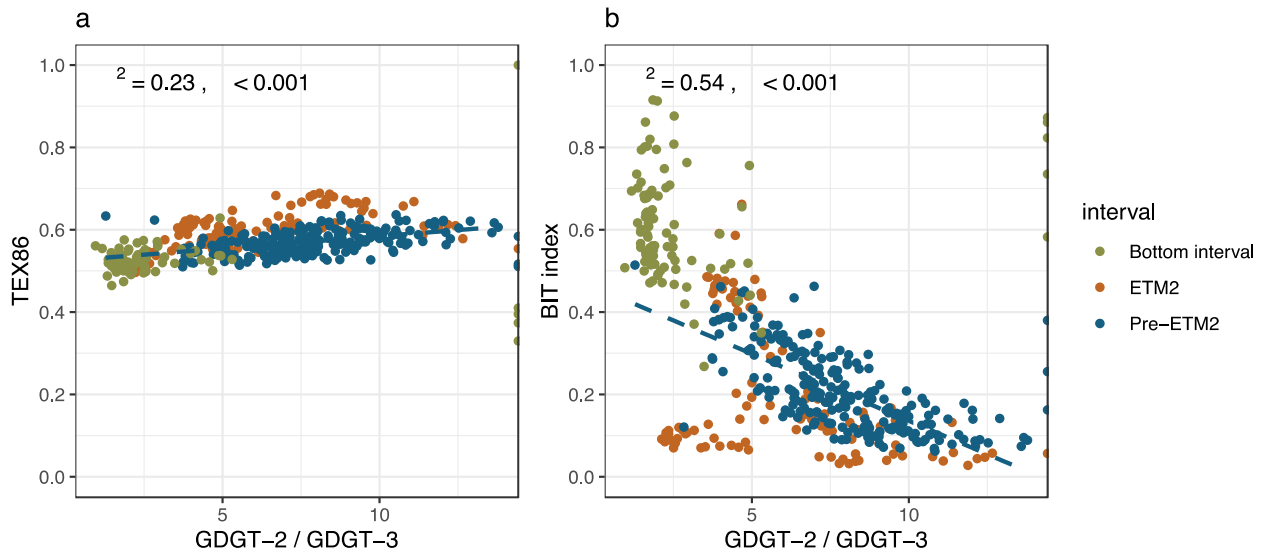


Figure S5. GDGT-2/GDGT-3 versus TEX₈₆ (a) and BIT index (b). Colors mark intervals, as distinguished in Main Text Section 3.1. Linear regression (blue dashed line), with its R-squared and P-values are displayed exclusively for the PreETM2 interval.

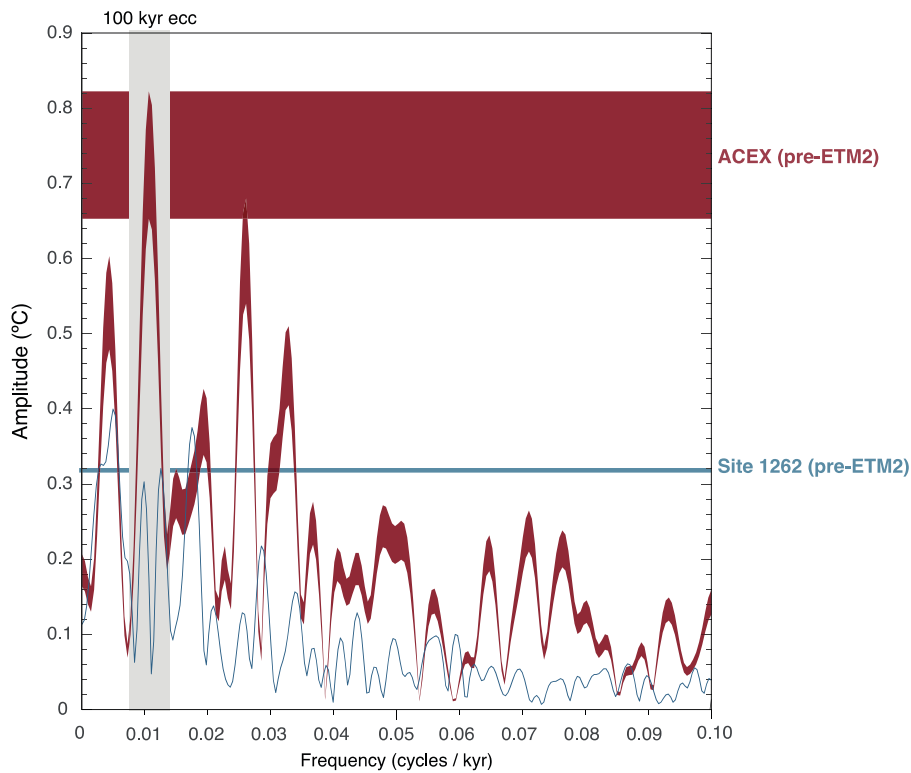


Figure S6. Amplitude comparison of ~100 kyr eccentricity-forced temperature variability between the ACEX and Site 1262 during the pre-ETM2 interval (54.1–54.5 Ma). Uncertainty range in the ACEX estimate represents the difference between SST (TEX_{86}^H , highest amplitude) and SubT ($SubT_{100-250m}$, lowest amplitude) TEX_{86} calibrations.